
The Symmetry of Electron Diffraction Zone Axis Patterns

B. F. Buxton, J. A. Eades, J. W. Steeds and G. M. Rackham

Phil. Trans. R. Soc. Lond. A 1976 **281**, 171-194

doi: 10.1098/rsta.1976.0024

Email alerting service

Receive free email alerts when new articles cite this article - sign up in the box at the top right-hand corner of the article or click [here](#)

THE SYMMETRY OF ELECTRON DIFFRACTION ZONE AXIS PATTERNS

BY B. F. BUXTON, J. A. EADES, J. W. STEEDS

AND G. M. RACKHAM

H. H. Wills Physics Laboratory, Tyndall Avenue, Bristol BS8 1TL

(Communicated by F. C. Frank, F.R.S. – Received 8 August 1975)

[Plates 1–3]

CONTENTS

	PAGE
1. INTRODUCTION	172
2. THEORY	172
(<i>a</i>) Outgoing solutions and reciprocity	173
(<i>b</i>) Effect of space group symmetry	174
(<i>c</i>) The thirty-one diffraction groups	176
(<i>d</i>) The projection approximation and systematic diffraction	177
(<i>e</i>) Symmetry of convergent beam patterns	178
(<i>f</i>) Symmetry of lattice images	179
3. A GRAPHICAL METHOD	180
4. THE DIFFRACTION GROUPS	186
5. EXPERIMENTAL RESULTS	190
6. DISCUSSION AND CONCLUSIONS	192
REFERENCES	193

The convergent beam and bend extinction contour techniques of electron microscopy are capable of providing much more information than can be obtained from conventional diffraction patterns and it is the objective of this work to examine the symmetry properties of each of these patterns. The diffraction of fast electrons by a thin parallel-sided slab has been studied by group theory and by a graphical construction. We find that the pattern symmetries may be described by thirty-one diffraction groups and that each of these diffraction groups is isomorphic to one of the point groups of diperiodic plane figures and to one of the thirty-one Shubnikov groups of coloured plane figures.

A graphical representation of each diffraction group is given, together with tables showing how the diffraction groups are related to the specimen point groups and under certain assumptions to the crystal point groups. These tables assume the symmetric Laue condition and ignore the presence of irreducible lattice translations normal to the slab. By using the tables, crystal point groups can be obtained from convergent beam or bend contour patterns. The method is demonstrated by experiments on several materials, but particularly on germanium and gallium-arsenide specimens since the similarity of these materials exemplifies the sensitivity of the technique.

1. INTRODUCTION

Electron diffraction as a technique for crystallographic analysis has been relatively little used in the past because it has often been regarded as a modified form of X-ray diffraction with added complications and limitations. In this paper we attempt to demonstrate that, far from being an impoverished form of X-ray diffraction, electron diffraction is a powerful tool for deducing crystal symmetries, sometimes in a more simple and direct fashion than can otherwise be achieved.

It has long been recognized that as electron diffraction does not obey Friedel's rule it can be used to investigate the presence of an inversion centre in a crystal. The many papers on this subject have been reviewed by Cowley (1967) and Uyeda (1974). However, the determination of symmetry from conventional electron diffraction patterns is severely hampered by the almost inevitable variation of thickness or orientation of the diffracting specimen. One way of overcoming this difficulty relies on contrast changes across twin boundaries in enantiomorphic crystals (Tanaka & Honjo 1964; Tanaka 1975) but it was not until the development of the convergent beam technique, where the illuminated area may be only 10 nm in diameter, that symmetry properties could be carefully investigated (Goodman & Lempfuhr 1968). The convergent beam diffraction patterns show a great wealth of detail which we believe is not greatly affected by inelastic and diffuse scattering in distinct contrast to the better known Kikuchi (Thomas 1970) and Coates (Joy 1974) patterns. It is only surprisingly recently that it has been recognized that bend extinction contour patterns may also be used for the careful examination of crystal symmetries (Steeds, Tatlock & Hampson 1973). This method relies on the eye's ability at pattern recognition to pick out symmetry properties of the distorted patterns which are normally obtained.

In this paper we give the derivation of tables of diffraction symmetries of bend contour and convergent beam patterns under the assumption of plane parallel sided regions of specimens with illumination incident approximately normal to the surface. Both group theoretical and diagrammatic derivations are presented and the results illustrated by a number of examples.

2. THEORY

Following Tournarie (1961, 1962) and Kambe (1967) we suppose that the incident electron beam may be represented as a plane wave which impinges on a thin, perfect, crystalline slab (figure 1*a*). This slab is to be regarded as cut from an infinite perfect crystal so that it is infinite in transverse directions and has parallel plane surfaces which are perpendicular to the reciprocal lattice vector \mathbf{s} of the parent crystal. It is therefore invariant under a translation by any of the lattice vectors $\{\boldsymbol{\tau}\}$ parallel to its planar surfaces. Since the vectors $\{\boldsymbol{\tau}\}$ are a subset of the lattice vectors $\{\mathbf{l}\}$ of the parent crystal, it is easily shown that the net reciprocal to $\{\boldsymbol{\tau}\}$ may be generated by projecting the vectors $\{\mathbf{g}\}$, reciprocal to $\{\mathbf{l}\}$, into the surface plane. Denoting the projections of vectors into the surface plane by capitals, we have

$$\mathbf{G} \cdot \boldsymbol{\tau} = 2\pi n, \quad (2.1)$$

where n is an integer.

The solutions of the high energy Schrödinger equation (Fujiwara 1961, 1962)

$$[\nabla^2 + k^2 - U(\mathbf{r})] \Psi(\mathbf{r}) \equiv H\Psi(\mathbf{r}) = 0, \quad (2.2)$$

therefore satisfy a two dimensional version of Bloch's theorem (Kambe 1967). In the above, k is the wavenumber of the relativistic electrons of mass m and $U(\mathbf{r})$ is $2m/\hbar^2$ times the optical potential.

An optical potential must be used in (2.2) to allow for absorption of electrons from the coherent, elastically scattered waves due to inelastic processes (see, for example, Dederichs 1972; Howie & Stern 1972). In principle, this optical potential is a non-local operator which must, however, be symmetric in its position representation (Dederichs 1972). We use a local (and complex) approximation to the optical potential, as shown in equation (2.2). $U(\mathbf{r})$ is assumed to vanish outside the crystal slab, so that if the z axis is chosen parallel to \mathbf{s} as in figure 1, we can write,

$$U(\mathbf{r}) = U_c(\mathbf{r}) h(z), \quad (2.3)$$

where for a crystal of thickness t , the 'hat' function $h(z)$ is unity for $0 \leq z \leq t$ and zero elsewhere. $U_c(\mathbf{r})$ has the space group symmetry of the infinite crystal (Dederichs 1972). By using the convenient symbol $\{R|\mathbf{v}\}$ (Seitz 1936) to represent the transformation of coordinates

$$\mathbf{r}' = \{R|\mathbf{v}\} \mathbf{r} = R\mathbf{r} + \mathbf{v}, \quad (2.4)$$

(R represents a rotation or reflexion of the space group, hereafter referred to as a 'rotation' and \mathbf{v} represents a translation) and the function operator, the space group symmetry of $U_c(\mathbf{r})$ can be written as

$$\{R|\mathbf{v}\} U_c(\mathbf{r}) = U_c(R^{-1}(\mathbf{r} - \mathbf{v})) = U_c(\mathbf{r}). \quad (2.5)$$

In § 2 (b) below, we will discuss the consequences of this space group symmetry, but first we turn to the solutions of (2.2) and an extra symmetry inherent in that equation.

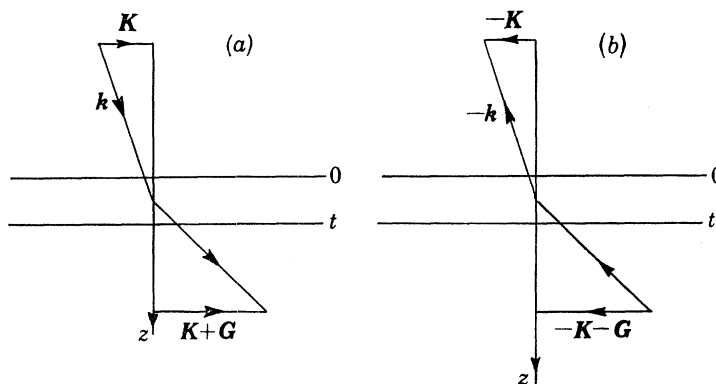


FIGURE 1. (a) Shows electrons with wavevector \mathbf{k} incident on the crystal slab from above; (b) shows the time reversed waves incident from beneath.

(a) *Outgoing solutions and reciprocity*

Defining

$$\Gamma_G(\mathbf{K}) = \begin{cases} \sqrt{(k^2 - (\mathbf{K} + \mathbf{G})^2)} & \text{if } k^2 \geq (\mathbf{K} + \mathbf{G})^2 \\ i\sqrt{((\mathbf{K} + \mathbf{G})^2 - k^2)} & \text{if } k^2 \leq (\mathbf{K} + \mathbf{G})^2 \end{cases}, \quad (2.6)$$

Kambe (1967) has shown that the outgoing solution of (2.2) for a plane wave $\exp(i\mathbf{k} \cdot \mathbf{r})$ incident from above may be written as,

$$\Psi_{\mathbf{K}}^{(+)} = e^{i\mathbf{K} \cdot \mathbf{R}} e^{i\Gamma_0(\mathbf{K})z} + \sum_{\mathbf{G}} R_{\mathbf{G}}^{(+)}(\mathbf{K}) e^{i(\mathbf{K} + \mathbf{G}) \cdot \mathbf{R}} e^{-i\Gamma_{\mathbf{G}}(\mathbf{K})z} \quad (2.7)$$

for $z < 0$; while for $z > t$ we have

$$\Psi_{\mathbf{K}}^{(+)} = \sum_{\mathbf{G}} T_{\mathbf{G}}^{(+)}(\mathbf{K}) e^{i(\mathbf{K} + \mathbf{G}) \cdot \mathbf{R}} e^{i\Gamma_{\mathbf{G}}(\mathbf{K})z}, \quad (2.8)$$

since $U(\mathbf{r})$ is zero in these regions. $R_{\mathbf{G}}^{(+)}(\mathbf{K})$ is the reflexion coefficient for the \mathbf{G} diffracted wave, and $T_{\mathbf{G}}^{(+)}(\mathbf{K})$ is the transmission coefficient. The (+) symbol attached to these quantities and the wave function shows that they refer to a wave incident *from above*. Similarly, for a wave $\exp[i(\mathbf{K} \cdot \mathbf{R} - \Gamma_0(\mathbf{K})z)]$ incident from below,

$$\Psi_{\mathbf{K}}^{(-)} = \sum_{\mathbf{G}} T_{\mathbf{G}}^{(-)}(\mathbf{K}) e^{i(\mathbf{K}+\mathbf{G}) \cdot \mathbf{R}} e^{-i\Gamma_{\mathbf{G}}(\mathbf{K})z} \quad (2.9)$$

for $z < 0$, and for $z > t$,

$$\Psi_{\mathbf{K}}^{(-)} = e^{i\mathbf{K} \cdot \mathbf{R}} e^{-i\Gamma_0(\mathbf{K})z} + \sum_{\mathbf{G}} R_{\mathbf{G}}^{(-)}(\mathbf{K}) e^{i(\mathbf{K}+\mathbf{G}) \cdot \mathbf{R}} e^{i\Gamma_{\mathbf{G}}(\mathbf{K})z}. \quad (2.10)$$

These solutions $\Psi^{(+)}$ and $\Psi^{(-)}$ would be related by time reversal symmetry if H were Hermitian (figure 1). Here, H is not Hermitian but it is symmetric in its position representation so we can still relate $\Psi^{(+)}$ and $\Psi^{(-)}$ by using reciprocity (Billhorn *et al.* 1964). Explicitly, we begin with the identity

$$0 \equiv \int_{\text{slab}} d^3\mathbf{r} [\Psi_{\mathbf{K}}^{(+)}(\mathbf{r}) k^2 \Psi_{\mathbf{K}'}^{(-)}(\mathbf{r}) - \Psi_{\mathbf{K}'}^{(-)}(\mathbf{r}) k^2 \Psi_{\mathbf{K}}^{(+)}(\mathbf{r})], \quad (2.11)$$

and use the Schrödinger equation (2.2), Bloch's theorem and the matching conditions on the wavefunction and its derivative on the surfaces of the slab (see Kambe 1967 for these boundary conditions) to show that

$$\Gamma_{\mathbf{G}}(\mathbf{K}) T_{\mathbf{G}}^{(+)}(\mathbf{K}) = \Gamma_{\mathbf{G}}(-\mathbf{K} - \mathbf{G}) T_{\mathbf{G}}^{(-)}(-\mathbf{K} - \mathbf{G}). \quad (2.12)$$

For high energy electrons incident nearly normally on the slab (so that $|\mathbf{K}| \ll k$) only those diffracted waves making small angles with the incident direction carry any appreciable flux. Both $\Gamma_{\mathbf{G}}(\mathbf{K})$ and $\Gamma_0(\mathbf{K})$ are very nearly equal to k for these waves, and our reciprocity relation in this forward scattering approximation becomes:

$$T_{\mathbf{G}}^{(+)}(\mathbf{K}) = T_{\mathbf{G}}^{(-)}(-\mathbf{K} - \mathbf{G}). \quad (2.13)$$

The reciprocity relation (2.12) is equivalent to the more familiar form used by Pogany & Turner (1968). Although they were able to make some remarks about the diffuse and inelastically scattered electrons (which are not considered here), they do not systematically study the effects of the space group symmetry of the crystal. Our present model, however, has been chosen to facilitate this task.

(b) *Effect of the space group symmetry*

If the potential $U(\mathbf{r})$ is invariant under an operation $\{R|\mathbf{v}\}$, then $\{R|\mathbf{v}\}\Psi$ will be a solution of the Schrödinger equation (2.2). However, not all space group symmetry operations of $U_c(\mathbf{r})$ leave $U(\mathbf{r})$ unchanged. The presence of the surfaces means that we must have transformations (2.4) with $z' = z$ or $z' = -z + t$ if $U(\mathbf{r})$ is to remain unchanged.

If the former condition applies, only symmetry operators which leave the surfaces of the slab unchanged have to be considered. If \mathcal{R} is a 'rotation' in this plane about the z axis and \mathbf{V} is a translation also in the plane, we may partition the Seitz symbol so that

$$R = \left(\begin{array}{c|c} \mathcal{R} & \mathbf{0} \\ \hline \mathbf{0} & 1 \end{array} \right) \quad \text{and} \quad \mathbf{v} = (\mathbf{V}, 0). \quad (2.14)$$

In the latter case, the operators have to be partitioned as

$$R' = \left(\begin{array}{c|c} \mathcal{R}' & \mathbf{0} \\ \hline \mathbf{0} & -1 \end{array} \right) \quad \text{and} \quad \mathbf{v}' = (\mathbf{V}', t). \quad (2.15)$$

We have used the primes, here and throughout § 2, to indicate that the crystal has been turned over.

The restrictions imposed by (2.14) and (2.15) must be considered carefully. First, symmetry operations are defined in terms of *lattice* directions, whereas the axis z is referred to a *reciprocal* lattice direction. In general a lattice direction will not be parallel to a reciprocal lattice direction, although there are special directions which are parallel to both a lattice vector and a reciprocal lattice vector. In particular, if the z axis is a rotation axis (of order ≥ 2) or is perpendicular to a mirror plane, then this axis will be both a lattice and a reciprocal lattice direction and the condition of the symmetric Laue case is satisfied (Fukuhara 1966). However, if a diad axis or mirror normal lies in the surface plane, or if the only non-trivial symmetry operation satisfying (2.14) and (2.15) is an inversion centre, the surface normal \mathbf{s} need not be parallel to a lattice direction. In this case we shall assume that no significant error will be introduced by using a zone axis \mathbf{u} , which is very nearly parallel to \mathbf{s} , to designate the direction of z . This will be advantageous later when we make the *projection approximation* and consider only diffraction processes related to the zero layer of the reciprocal lattice for which $\mathbf{g} \cdot \mathbf{u}$ is zero (Howie 1966; Fukuhara 1966; Pogany & Turner 1968; Berry 1971).

Secondly, according to (2.14) the rotation R can only be associated with a translation \mathbf{v} in the surface plane. Certainly, if the space group of the parent crystal is symmorphic (see, for example, Zachariasen 1945) we can always choose the translations \mathbf{v} ($= \boldsymbol{\tau}$) in this plane, but if it is asymmorphic, this will not always be so: for example, screw axes and glide planes with associated translations not parallel to the surfaces are here excluded. Similarly, R' must be an inversion axis parallel to z , or a diad or screw diad axis perpendicular to z , or a mirror or glide plane also perpendicular to z . Inversion axes have no associated fractional lattice translations, so the second part of (2.15) means that the thickness t must be the z -component of a lattice translation. This is also the case if R is a twofold operation normal to z which does not have an associated fractional translation along the z axis. However, as Goodman points out (Goodman 1974), a mirror perpendicular to z is a possible symmetry operation even if t is not the z -component of a lattice translation. The important point is only that the slab of crystal should be invariant under the operation considered; for example, the mid-plane of the crystal can be a mirror or glide plane, or there can be a twofold rotation axis in the mid-plane. Because of these complications, we shall assume that $\{R|\mathbf{v}\}$ and $\{R'|\mathbf{v}'\}$ as given by (2.14) and (2.15) are symmetry operations of the crystal slab and focus our attention on the point group operations R and R' . The partitioned form of these operators makes it clear (see for instance the comments in the preface of Shubnikov 1964) that the thirty-one distinct point groups constructed from R and R' will be isomorphic to the crystallographic point groups of two dimensional plane figures (see Shubnikov 1964 or Megaw 1973 for instance).

Applying an operator $\{R|\mathbf{v}\}$ given by (2.14) to the wave function $\Psi_{\mathbf{K}}^{(+)}$, we find for $z < 0$ that,

$$e^{i\mathcal{R}\mathbf{K} \cdot \mathbf{V}} \{R|\mathbf{v}\} \Psi_{\mathbf{K}}^{(+)}(\mathbf{r}) = e^{i\mathcal{R}\mathbf{K} \cdot \mathbf{R}} e^{i\Gamma_0(\mathcal{R}\mathbf{K})z} + \sum_{\mathbf{G}} (R_{\mathcal{R}\mathbf{G}}^{(+)}(\mathbf{K}) e^{-i\mathbf{G} \cdot \mathbf{V}}) e^{i(\mathcal{R}\mathbf{K} + \mathbf{G}) \cdot \mathbf{R}} e^{-i\Gamma_{\mathbf{G}}(\mathcal{R}\mathbf{K})z}. \quad (2.16)$$

Since the outgoing solution of (2.2) with an incident plane wave is unique, comparison of (2.16) and (2.7) shows that:

$$R_{\mathbf{G}}^{(+)}(\mathbf{K}) = e^{i\mathcal{R}\mathbf{G} \cdot \mathbf{V}} R_{\mathcal{R}\mathbf{G}}^{(+)}(\mathcal{R}\mathbf{K}) \quad (2.17)$$

and that

$$\Psi_{\mathcal{R}\mathbf{K}}^{(+)}(\mathbf{r}) = e^{i\mathcal{R}\mathbf{K} \cdot \mathbf{V}} \{R|\mathbf{v}\} \Psi_{\mathbf{K}}^{(+)}(\mathbf{r}). \quad (2.18)$$

Equation (2.18) shows that $\Psi_{\mathbf{K}}^{(+)}(\mathbf{r})$ behaves in an analogous way to a non-degenerate Bloch function of a three dimensionally infinite crystal. Moreover, using (2.18) and the expressions for $\Psi_{\mathbf{K}}^{(+)}(\mathbf{r})$ and $\Psi_{\mathcal{R}\mathbf{K}}^{(+)}(\mathbf{r})$ in the region $z > t$, we see that

$$T_{\mathbf{G}}^{(+)}(\mathbf{K}) = e^{i\mathcal{R}\mathbf{G}\cdot\mathbf{V}} T_{\mathcal{R}\mathbf{G}}^{(+)}(\mathcal{R}\mathbf{K}). \quad (2.19)$$

In the same way, we can use an operator $\{R'|\mathbf{v}'\}$ given by (2.15), and deduce that

$$\Psi_{\mathcal{R}'\mathbf{K}}^{(-)}(\mathbf{r}) = e^{i\mathcal{R}'\mathbf{K}\cdot\mathbf{V}'} e^{-i\Gamma_0(\mathcal{R}'\mathbf{K})t} \{R'|\mathbf{v}'\} \Psi_{\mathbf{K}}^{(+)}(\mathbf{r}), \quad (2.20)$$

and that,

$$T_{\mathbf{G}}^{(+)}(\mathbf{K}) = e^{i\mathcal{R}'\mathbf{G}\cdot\mathbf{V}'} e^{i(\Gamma_0(\mathbf{K})-\Gamma_0(\mathcal{R}'\mathbf{K}))t} T_{\mathcal{R}'\mathbf{G}}^{(-)}(\mathcal{R}'\mathbf{K}). \quad (2.21)$$

Combining this with the reciprocity theorem (2.13), we see that for near forward scattering:

$$T_{\mathbf{G}}^{(+)}(\mathbf{K}) = e^{i\mathcal{R}'\mathbf{G}\cdot\mathbf{V}'} e^{i(2\mathbf{K}\cdot\mathbf{G}+G^2)t/2k} T_{\mathcal{R}'\mathbf{G}}^{(+)}(-\mathcal{R}'(\mathbf{K}+\mathbf{G})). \quad (2.22)$$

Equations (2.19) and (2.22) together express the effect of the various symmetry operations of the crystal slab on the diffracted waves.

(c) The thirty-one diffraction groups

We have already remarked that thirty-one Shubnikov plane crystallographic point groups can be constructed from the sets of operators $\{R\}$ and $\{R'\}$ given by (2.14) and (2.15). We shall now show how these operators give rise to thirty-one isomorphic groups of symmetry operators on the diffracted waves. First, it is convenient to remove the translational part from the argument of the transmission coefficient on the right of (2.22) by referring all orientations with respect to the Bragg positions, that is, we define

$$\mathbf{K} = -\frac{1}{2}\mathbf{G} + \mathbf{Q}. \quad (2.23)$$

Furthermore, a very long way beyond the crystal slab (or in the back focal plane of the objective lens of a microscope) the transmitted diffracted waves are well separated and each carries a current proportioned to $|T_{\mathbf{G}}^{(+)}(\mathbf{K})|^2$. We therefore define $I(\mathbf{G}, \mathbf{Q})$ as the intensity in the \mathbf{G} th diffracted beam at an orientation \mathbf{Q} from the \mathbf{G} Bragg position, so that,

$$I(\mathbf{G}, \mathbf{Q}) = |T_{\mathbf{G}}^{(+)}(-\frac{1}{2}\mathbf{G} + \mathbf{Q})|^2. \quad (2.24)$$

Our symmetry relations (2.19) and (2.22) then mean that:

$$I(\mathbf{G}, \mathbf{Q}) = I(\mathcal{R}\mathbf{G}, \mathcal{R}\mathbf{Q}) = I(\mathcal{R}'\mathbf{G}, -\mathcal{R}'\mathbf{Q}). \quad (2.25)$$

Introducing a new symmetry operator $\{\mathcal{P}, \pm 1\}$ which acts on a function $F(\mathbf{G}, \mathbf{Q})$ so that,

$$\{\mathcal{P}, \pm 1\}F(\mathbf{G}, \mathbf{Q}) = F(\mathcal{P}^{-1}\mathbf{G}, \pm \mathcal{P}^{-1}\mathbf{Q}), \quad (2.26)$$

(cf. the action of the Seitz operator, equation (2.5)) it is not hard to show from the point group properties of $\{R\}$ and $\{R'\}$ (or indeed $\{\mathcal{R}\}$ and $\{\mathcal{R}'\}$) that operators $\{\mathcal{R}, 1\}$ and $\{\mathcal{R}', -1\}$ can be used to construct thirty-one groups which are isomorphic to the Shubnikov groups mentioned above. This task is much simplified by noting that the symmetry of the specimen slab must itself be one of the 31 point groups of di-periodic plane figures (§ 2 (b)) which are isomorphic to the Shubnikov groups. From the form of (2.26) we now see that the possible symmetry properties of the diffracted wave intensities as represented by (2.25), must be one of these thirty-one groups, here called *diffraction groups*. In table 1 we present a pictorial representation of the diffracted wave intensities and in § 3, a geometrical interpretation of the operators $\{\mathcal{R}, 1\}$ and $\{\mathcal{R}', -1\}$. Since this interpretation is not the same as a colour change, we introduce a new notation for these operations on the

diffracted wave intensities, which however preserves the isomorphism with the Shubnikov groups. Table 3 also contains a list of the diffraction groups and details of how they are related, via conditions (2.14) and (2.15), to the point groups of the parent crystal.

The diffraction group is determined in any particular case by requiring that the intensity $I(\mathbf{G}, \mathbf{Q})$ be invariant under *all* operations of the group for a general \mathbf{G} and \mathbf{Q} . For special choices of \mathbf{G} and \mathbf{Q} the symmetry may of course appear different from that of the diffraction group. If it happens that a particular \mathbf{G} vector is chosen for which, say, $\mathcal{R}\mathbf{G}$ or $\mathcal{R}'\mathbf{G}$ is identically \mathbf{G} itself for some operator \mathcal{R} or \mathcal{R}' , then (2.25) shows that there is an internal symmetry relation concerning this diffracted beam alone. The direct (zero) beam always behaves in this anomalous way: for instance the presence of an inversion centre of symmetry in the zero beam will result from (for example) either a diad axis parallel to z (an \mathcal{R} operation) or by a mirror perpendicular to z (an \mathcal{R}' operation) (cf. Goodman & Steeds 1975).

(d) *The projection approximation and systematic diffraction*

Although the z dependence of the potential $U(\mathbf{r})$ can give rise to dramatic and useful effects such as upper layer lines (Rackham, Jones & Steeds 1974), it often happens when z is parallel to a prominent zone axis \mathbf{u} , and \mathbf{K} is small, that all the observable features of the diffraction are due to interactions related to the zero layer of the reciprocal lattice. In this case, we consider the projected potential $\bar{U}_c(\mathbf{R})$, obtained by averaging $U_c(\mathbf{r})$ over z (Berry 1971) so that,

$$\bar{U}_c(\mathbf{R}) = \sum_{\mathbf{0g}} U_{\mathbf{0g}} e^{i\mathbf{0g} \cdot \mathbf{R}}, \quad (2.27)$$

where the vectors $\mathbf{0g}$, perpendicular to \mathbf{u} form the zero layer of the reciprocal lattice. The space group symmetry of $U_c(\mathbf{r})$ means that we can write,

$$U_{\bar{\mathcal{R}}\mathbf{0g}} = U_{\mathbf{0g}} e^{-i\bar{\mathcal{R}}\mathbf{0g} \cdot \bar{\mathbf{V}}}, \quad (2.28)$$

where the set of 'rotations' $\{\bar{\mathcal{R}}\}$ includes the 'rotations' $\{\mathcal{R}\}$ and $\{\mathcal{R}'\}$ defined by (2.14) and (2.15), and the translations $\{\bar{\mathbf{V}}\}$ similarly include all the $\{\mathbf{V}\}$ and $\{\mathbf{V}'\}$. Ignoring accidental symmetries, (2.28) shows that the set of operators $\{\bar{\mathcal{R}}|\bar{\mathbf{V}}\}$ is the two dimensional space group of $\bar{U}_c(\mathbf{R})$. The scattering potential in (2.2) should now be replaced by $\bar{U}(\mathbf{r})$ which is equal to $\bar{U}_c(\mathbf{R})h(z)$. This is invariant under $\{\bar{\mathcal{R}}|\bar{\mathbf{V}}\}$ followed by a mirror reflexion in the plane $z = \frac{1}{2}t$, as well as under $\{\bar{\mathcal{R}}|\bar{\mathbf{V}}\}$ alone. The diffraction group is therefore composed of the sets of operators $\{\bar{\mathcal{R}}, 1\}$ and $\{\bar{\mathcal{R}}, -1\}$, or, equivalently the direct product $\{\{\bar{\mathcal{R}}, 1\} \otimes \{\mathcal{E}, \pm 1\}\}$ (\mathcal{E} is the two dimensional identity operator), which is isomorphic to one of the ten two dimensional grey point groups.

The fact that there are only ten distinct diffraction groups in this approximation reflects the considerable loss of information when the upper layer interactions are not observed. However, the combination of observations from a number of zone axes allows all but two (4 and $\bar{4}$) of the point group symmetries of the infinite crystal to be distinguished. Also, since the symmetry operation $\{\mathcal{E}, -1\}$ is always present in these direct product diffraction groups (hereafter referred to as projection diffraction groups),

$$I(\mathbf{G}, \mathbf{Q}) = I(\mathbf{G}, -\mathbf{Q}), \quad (2.29)$$

so that the diffracted wave intensities always possess inversion symmetry about the Bragg position, as noted by Pogany & Turner (1968).

Similarly, under systematic diffracting conditions when only interactions associated with one row of reciprocal vectors $\{n\mathbf{g}\}$, parallel to the x axis (say), are important, a one dimensional

potential $\bar{U}_c(x)$ analogous to $\bar{U}_c(\mathbf{R})$ can be defined (Berry 1971). $\bar{U}(\mathbf{r})$ is again $\bar{U}_c(x)h(z)$ and there remain only two diffraction groups (1_R and 21_R of table 1) which are isomorphic to the two one dimensional grey point groups. Only the component \mathbf{q}_x of \mathbf{Q} parallel to x is significant, so that if $\bar{U}_c(x)$ has an inversion centre we can write the symmetry properties as

$$I(n\mathbf{g}, \mathbf{q}_x) = I(n\mathbf{g}, -\mathbf{q}_x) = I(-n\mathbf{g}, -\mathbf{q}_x), \quad (2.30)$$

while in the absence of an inversion centre, only the first of these relations holds.

(e) *Symmetry of convergent beam patterns*

The symmetry of dark field patterns which are an essential part of the diffraction group can only be observed when the incident beam varies over a range including the relevant Bragg orientation. These large angular ranges are frequently obtained in bend contour work (Steeds *et al.* 1973). However, the convergent beam technique, which is useful for less buckled specimens, only allows a small range of incident orientations if different diffraction orders are not to overlap (figure 2). The entire region near a zone axis can of course be mapped out by using a series of these patterns taken by successively tilting the incident convergent beam (Goodman 1974) and the diffraction group inferred from the composite pattern.

However, if the mean incident direction is parallel to the z axis the normal convergent beam pattern still contains useful symmetry information. Electrons incident from different directions in the convergent beam are normally incoherent so the intensity observed in the convergent beam pattern in the back focal plane of the objective can be written as (see figure 2)

$$I(\mathbf{Q}) = \text{const.} \sum_{\mathbf{G}} |T_{\mathbf{G}}^{(+)}(\mathbf{Q} - \mathbf{G})|^2 F(|\mathbf{Q} - \mathbf{G}|), \quad (2.31)$$

where $F(|\mathbf{Q} - \mathbf{G}|)$ represents the incident electron intensity from a direction $\mathbf{Q} - \mathbf{G}$.

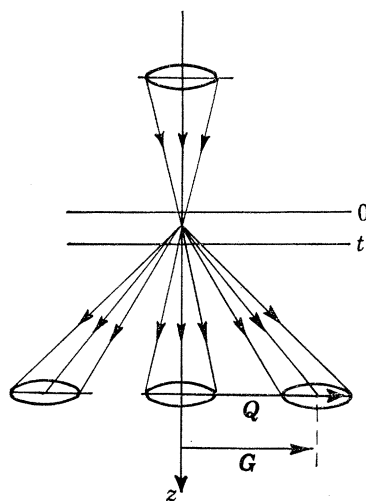


FIGURE 2. Schematic arrangement for the formation of a convergent beam pattern showing how the orientation vectors are defined.

For a conventional non-overlapping convergent beam pattern, $F(|\mathbf{Q}'|)$ is zero for large $|\mathbf{Q}'|$ so that only one diffracted wave contributes to the intensity $I(\mathbf{Q})$ at any \mathbf{Q} . From (2.19), it follows that $I(\mathbf{Q})$ is invariant under any of the rotation operations \mathcal{R} , but it is *not* invariant under the operations \mathcal{R}' which are associated with turning the crystal slab over. The symmetry of the whole

convergent beam pattern is therefore one of the ten two dimensional point groups. This point group is easily obtained from the diffraction group by removing all operations associated with turning the slab over, as shown in table 2. In the projection approximation the symmetry of the convergent beam pattern is just the point group $\{\mathcal{R}\}$ of the projected potential.

The zero beam of the convergent beam pattern should be treated separately, however (Goodman 1974), because this often shows an internal symmetry which is higher than that of the whole pattern. Assuming that the objective aperture is chosen so that only the zero beam is observed, the convergent beam pattern (2.31) becomes

$$I(\mathbf{Q}) = \text{const.} |T_0^{(+)}(\mathbf{Q})|^2 F(|\mathbf{Q}|). \quad (2.32)$$

Inspection of (2.19) and (2.22) now shows that the zero beam pattern is invariant under the rotations $\{\mathcal{R}\}$ and $\{\mathcal{R}'\}$, and it is easy to infer the zero beam point group symmetry from the diffraction group (see table 2). In particular, in the projection approximation,

$$T_0^{(+)}(\mathbf{Q}) = T_0^{+}(-\mathbf{Q}) \quad (2.33)$$

so that the zero beam pattern always possesses an inversion centre, even if the point group of the whole pattern does not (Goodman 1974).

Finally, we emphasize some of the assumptions used in the above discussion. First, it was assumed that the convergent beam illumination was symmetric about the z direction. If tilted illumination is used, centred on \mathbf{Q}_c (say), the incident distribution $F(|\mathbf{Q} - \mathbf{G}|)$ in (2.31) is replaced by $F(|\mathbf{Q} - \mathbf{G} - \mathbf{Q}_c|)$ and the intensity $I_{\mathbf{Q}_c}(\mathbf{Q})$ of this convergent beam pattern is equal to the intensity $I_{\mathcal{R}\mathbf{Q}_c}(\mathcal{R}\mathbf{Q})$ of the convergent beam pattern obtained with the illuminating cone centred on $\mathcal{R}\mathbf{Q}_c$. Indeed, if the illuminating cone is tilted far enough towards the Bragg position for a particular dark field, it is often possible to deduce from this dark field convergent beam disk the full diffraction group symmetry. Secondly, it has been assumed that the incident intensity distribution $F(|\mathbf{Q}'|)$ is symmetric, but this will not be the case if the probe forming lens system introduces appreciable astigmatism or coma.

(f) Symmetry of lattice images

From equation (2.18) of § 2 (b) we see that, for electrons incident normally from above, the wave function $\Psi_0^{(+)}(\mathbf{R}, t)$ on the exit face of the crystal slab is invariant under the symmetry operations $\{\mathcal{R}|V\}$ which transform $\Psi_0^{(+)}(\mathbf{R}, t)$ to $\Psi_0^{+}(\mathcal{R}^{-1}(\mathbf{R} - V), t)$. This indicates that lattice images provide information about the *space group* of the parent crystal. However, we must include some of the effects of the principal aberrations of the electron lenses, in particular the objective lens, and also any defocus. The object is the wave function $\Psi_0^{+}(\mathbf{R}, t)$ of the electrons on the exit face of the slab, which may be obtained from (2.8), so that the image wave function $\Phi_0(\mathbf{P}, \Delta)$ obtained with an overfocus Δ is given by (see, for example, Lenz 1971)

$$\Phi_0(\mathbf{P}, \Delta) = \sum_{\mathbf{G}} T_{\mathbf{G}}^{(+)}(0) e^{i\Gamma_{\mathbf{G}}(0)t} e^{-iW(\mathbf{G}, \Delta)} D(|\mathbf{G}|) e^{i\mathbf{G} \cdot \mathbf{P}/M}. \quad (2.34)$$

Here, $D(|\mathbf{G}|)$ is the aperture function for an objective aperture symmetrically placed about the optic axis which coincides with the z axis. M is the magnification of the image and, if spherical aberration and axial astigmatism are included (Lenz 1971)

$$W(\mathbf{G}, \Delta) = \frac{c_S}{4k^3} G^4 + \frac{\Delta}{2k} G^2 - \frac{c_A}{2k} (G_X^2 - G_Y^2), \quad (2.35)$$

where c_S is the third order spherical aberration coefficient and c_A is the coefficient of astigmatism referred to principal axes X and Y of the electron optical system.

Because of the magnification factor M , we now consider the action of an operator $\{\mathcal{R}|MV\}$ on the image wave function $\Phi_0(\mathbf{P}, \Delta)$. This is transformed into $\Phi_0(\mathcal{R}^{-1}(P - MV), \Delta)$, so it is easily seen from (2.19) and (2.34) that the image wavefunction $\Phi_0(\mathbf{P}, \Delta)$ remains unchanged, if there is no astigmatism. The lattice image $|\Phi_0(\mathbf{P}, \Delta)|^2$ therefore possesses the symmetry of the space group operations $\{\mathcal{R}|V\}$ of the parent crystal. If the projection approximation is valid, this is just the space group $\{\mathcal{R}|\bar{V}\}$ of the projected potential $\bar{U}_c(\mathbf{R})$. (An example of this may be found in Iijima (1971), while a table of some projected space groups can be found in Buerger (1960), ch. 11.) We emphasize that this is independent of spherical aberration and defocus, but depends on a symmetrically placed aperture and on the specimen slab being normal to the optic axis. Moreover, for more general apertures which admit only a few diffracted beams, it is possible that $\Phi_0(\mathbf{P}, \Delta)$ will show a higher symmetry than $\Psi_0^{(+)}(\mathbf{R}, t)$ (figure 3a), or a lower symmetry as in figure 3b. If the illumination is tilted, it turns out that the image wavefunction $\Phi_K(\mathbf{P}, \Delta)$ behaves similarly to the object wavefunction $\Psi_K^{(+)}(\mathbf{R}, t)$ as in (2.18). There are also similar symmetry relations involving the operations $\{\mathcal{R}'|V'\}$ related to the $\{\mathcal{R}'|v'\}$ of (2.15), but as in (2.20), these involve turning the slab over.

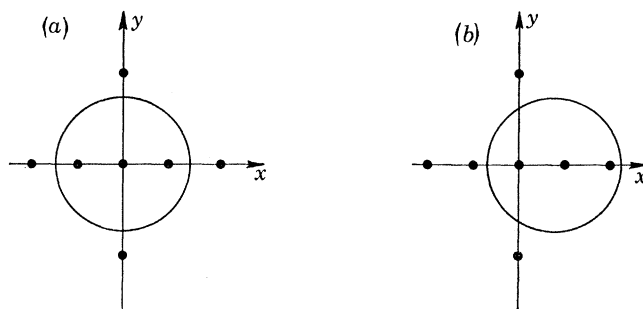


FIGURE 3. The large circle represents the aperture in the back focal plane of the objective lens, and it is assumed that $\Psi_0^{(+)}(\mathbf{R}, t)$ remains unchanged on reflexion in the y axis, i.e. $\Psi_0^{(+)}(x, y, t) = \Psi_0^{(+)}(-x, y, t)$, but $\Psi_0^{(+)}(x, y, t) \neq \Psi_0^{(+)}(x, -y, t)$. In (a) $\Phi_0(x, y, \Delta) = \Phi_0(-x, y, \Delta) = \Phi_0(x, -y, \Delta)$ and we obviously have no information on symmetry properties in the y direction, whereas in (b) the former symmetry is missing.

Finally, under stigmatic imaging conditions, most of the symmetry properties of $\Psi_0^{(+)}(\mathbf{R}, t)$ will not apply to $\Phi_0(\mathbf{P}, \Delta)$ because the phase change $-c_A(G_X^2 - G_Y^2)/2k$ will *not* be invariant under most operations defined with respect to axes x and y of the crystal, because these will not in general be parallel to the axes X and Y of the optical system. In general, $\Phi_0(\mathbf{P}, \Delta)$ will only be invariant under a twofold rotation about the z axis, when

$$\mathcal{R} = \begin{pmatrix} -1 & 0 \\ 0 & -1 \end{pmatrix}.$$

3. A GRAPHICAL METHOD

The way in which the specimen symmetry determines the symmetry in electron diffraction can readily be shown by a simple graphical method. In fact, the 31 diffraction groups were first determined by this method; the analysis of § 2 was used subsequently to confirm the results and explore their relations with other groups.

Previous workers looking for symmetry relations in diffraction have also used graphical methods but usually (e.g. figure 1, and also Pogany & Turner 1968) have employed ray diagrams projected onto a plane containing the incident beam. Such diagrams are only convenient in certain very simple cases. The advances which we report, have arisen, in no small measure, from the realization that the symmetry relations in diffraction are more readily explored by means of a stereographic projection in which the zone axis of interest is taken at the centre of the circle. Thus a single direct beam (as when no specimen is present or when diffracted beams are not considered) is illustrated in figure 4, where the cross marks the centre of the circle and hence represents the direction of the zone axis. The dot represents the ingoing ray and the circle the direction of the outgoing ray. In figure 5 *a* an additional dark-field is represented. In this diagram and throughout we assume that all the angles are small, that is, we take the diagrams to represent only small central regions of the stereographic projections. The ingoing and direct outgoing beams are unchanged but the direction of a second outgoing beam is represented by a circle displaced by twice the Bragg angle, in a direction parallel to the diffraction vector \mathbf{G} from the first. We find it convenient to identify this displacement by a vector \mathbf{G}' and to draw it from the centre of the circle as in figure 5 *b*; then the ingoing beam and the outgoing dark-field beam are symmetrical about the mid-point of \mathbf{G}' .

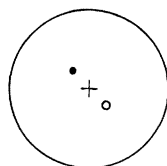


FIGURE 4. Stereographic projection of the directions of the ingoing and outgoing electron beams.

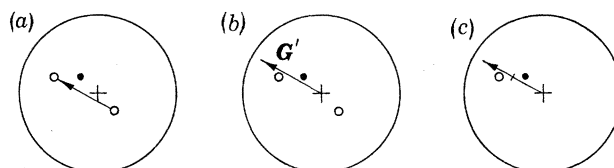


FIGURE 5. Stereographic projection: as figure 4 with the addition of a single diffracted beam.

The symmetries we are looking for are revealed as relations between the intensities of outgoing beams when we assume that the incident intensity is independent of orientation as in § 2 (*a*). (That is, we take all the incident beams to have unit intensity and look for specific orientations in which sets of outgoing beams have the same intensity.)

In order to simplify the diagrams it is convenient to consider dark- and bright-field images separately so that we usually put in only one emergent ray at a time and figure 5 *c* becomes a standard starting point for determining dark-field symmetries (figure 4 is the equivalent for bright field).

To show how the method works we first consider a simple example: let the specimen possess a mirror plane containing the zone axis and consider a pair of Bragg reflexions which are related by this mirror operation (figures 6 *a, b*), then if we introduce incident beams, also in mirror related positions, we get the result given in figures 6 *c, d*. Clearly the two outgoing rays have equal intensities (otherwise the mirror symmetry is destroyed). Hence in the dark-field images of mirror

related diffracted beams there are points which, for mirror related incident beams, must have equal intensity due to the symmetry.

We have now established the result we are looking for but we need both to examine what it means and to find a more convenient and readily interpretable way of representing it. If a dark-field image has internal symmetry the centre of the pattern is at the Bragg position which is represented by a small circle in figure 7 *a*; cf. § 2 (*c*). The Bragg condition is fulfilled anywhere along a line perpendicular to \mathbf{G} through this point and the dark-field intensity will be concentrated (if large enough angles are considered) along such a line. Therefore, the maximum symmetry of a dark-field image is the two dimensional crystallographic point group $2mm$ with the mirror planes parallel and perpendicular to \mathbf{G} .

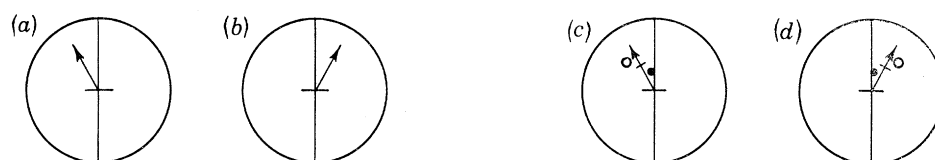


FIGURE 6. Derivation of the dark-field symmetry relation for a specimen with a vertical mirror.

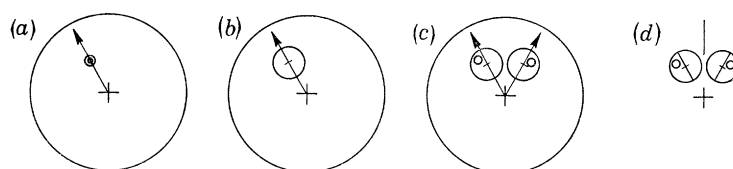


FIGURE 7. Stereograms showing (*a*) the centre of symmetry of the dark-field pattern and (*b*), (*c*) and (*d*) the development of the representation of the pattern symmetries.

Because the symmetry of the dark-field is centred on the point shown in figure 7 *a* we can conveniently represent the dark-field image as occurring within a circle centred on this point (figure 7 *b*). Then the result we have deduced for the mirror plane (figures 6 *c, d*) is represented by figure 7 *c* which is simplified to the diagram shown in 7 *d*. The 31 diffraction groups (§ 2 (*c*)) are tabulated in this form in table 1. We have dropped the dots once the final result has been obtained because we are no longer interested in the incident beam. However, we have included in figure 7 *d* a line above the centre, because if \mathbf{G} is parallel to it (or to any of the similar lines in table 1) a special result occurs. The diagram illustrates the relation only for a general \mathbf{G} and it would be too complicated to illustrate both special and general results. However, if the initial \mathbf{G} were taken parallel to the mirror plane, instead of obtaining a relation between different dark-field patterns, the result would be a mirror parallel to \mathbf{G} within that dark-field pattern. This result can be derived from following the argument illustrated in figure 6 or more quickly, from the general result shown in figure 7 *d*. In fact, all special results are easily derived from the general cases given in table 1.

Two further ideas are raised if we now consider a mirror plane perpendicular to the zone axis. Figure 8 *a* is the normal starting point, figure 8 *b* is the result of adding the mirror operation and figure 8 *c* represents the final result. We have jumped a step: in figure 8 *b* we have one downward going ray (the original one from 8 *a*) and one upward going ray (the one generated by the mirror operation). However we may use reciprocity to show that we can reverse this ray (see § 2 (*a*)) and

references made there). In fact the reciprocity theorem allows us to ignore the upward- or downward-going character of a ray and no distinguishing symbol is required. This is true regardless of what other beams are involved.

The second point of interest which arises from this example is that while the diagram of figure 8*c* has no overall symmetry (point group: 1) there is diad symmetry within each dark-field order (the diagram shows only one dark-field order because each dark-field image is unrelated to all the others but every dark-field image has its own internal twofold axis). We wish to develop a notation which allows us to represent the full symmetry including this internal symmetry of the dark-field orders. Either by considering each possible case in turn, or by using the group theoretical arguments given in previous sections, it can be shown that all the symmetries of the full pattern (dark- and bright-field images) can be described by means of a set of operations which includes only the operations of the two dimensional point groups and the same operations in combination with the additional special operator which rotates each dark-field through π about its own centre. We have designated the latter operator by the subscript R. Hence a horizontal mirror results in a diffraction group 1_R (figure 8*c*) and a vertical mirror in a diffraction group m (figure 7*d*).

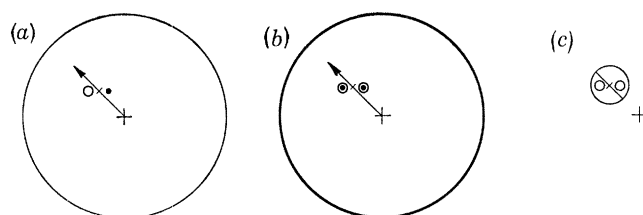


FIGURE 8. Development of the dark-field relation for a horizontal mirror.

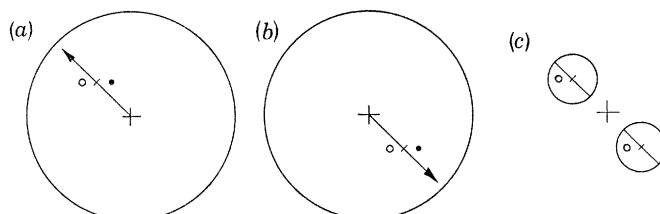


FIGURE 9. Development of the dark-field relation for a specimen with an inversion centre.

A particularly important case is that of a specimen with an inversion centre. Figure 9 illustrates the derivation and the result which reveals that in any crystal with an inversion centre each dark-field image (for a reflexion \mathbf{G}) is related to the dark-field image for $-\mathbf{G}$ by the operator 2_R illustrated in figure 9*c*. If this relation is found to be absent between $\pm \mathbf{G}$ images then the crystal cannot be centred; it will be seen that the operation 2_R consists in rotating through π about the centre of the pattern and also rotating each dark-field pattern through π about its own centre.

In this graphical approach, the 31 diffraction groups are generated by applying the method just described to every orientation of each of the 32 three dimensional point groups. Alternatively it has been noted (§ 2 (*b*)) that the specimen (as distinct from the infinite crystal) can only have one of the point groups of diperiodic plane figures and the method need only be applied to them.

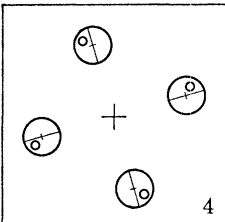
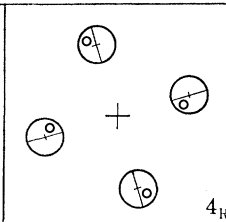
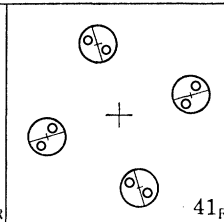
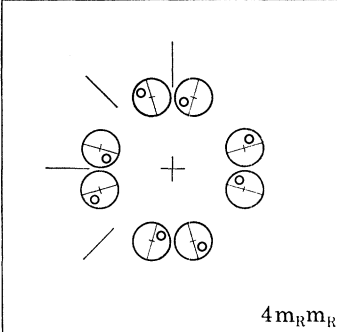
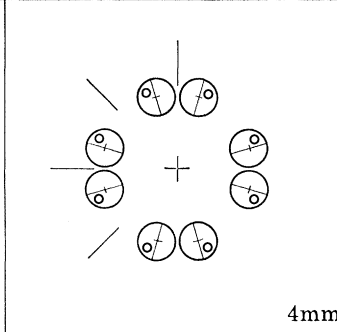
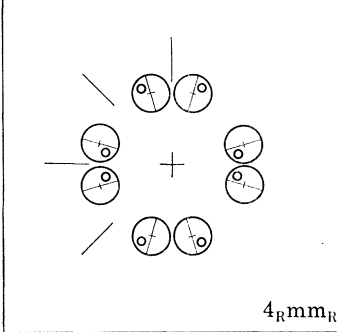
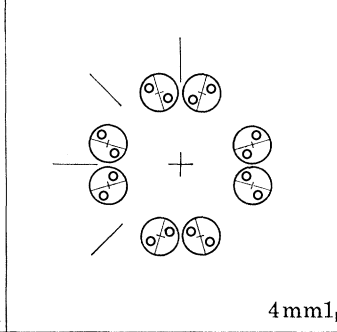
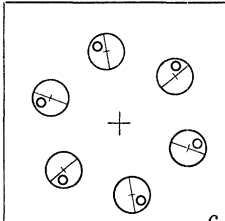
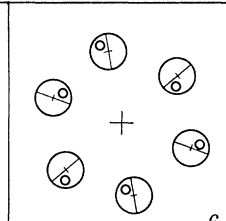
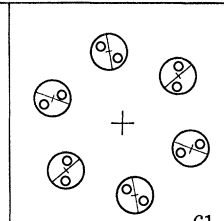
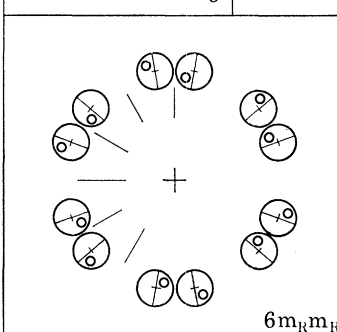
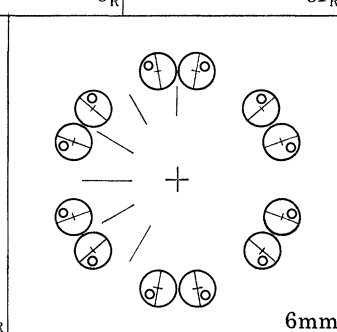
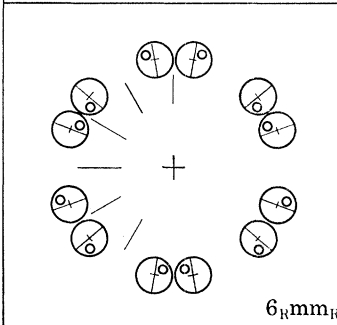
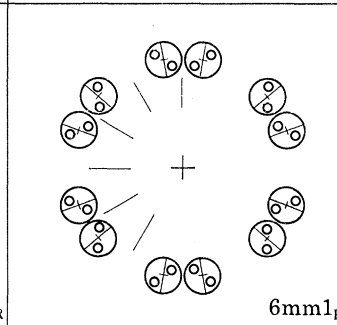
TABLE 1. GRAPHICAL REPRESENTATION OF THE DIFFRACTION GROUPS

 + 1	 + 1 _R	 — + 2m _R m _R
 + 2	 — + m _R	 — + 2mm
 + 2 _R	 — + m	 — + 2 _R mm _R
 + 21 _R	 — + m1 _R	 — + 2mm1 _R
 3		 31 _R
 3m _R		 3m
 3m1 _R		

ELECTRON DIFFRACTION SYMMETRIES

185

TABLE 1 (cont.)

 4	 4 _R	 4I _R
 4m _R m _R		 4mm
 4 _R mm _R		 4mmI _R
 6	 6 _R	 6I _R
 6m _R m _R		 6mm
 6 _R mm _R		 6mmI _R

4. THE DIFFRACTION GROUPS

We now present the results of carrying through the operations just described. Table 1 gives the graphical representation of the 31 diffraction groups. As already discussed each diagram represents the symmetry relations between general dark-field orders. The radial lines represent directions in which special relations hold, that is, when either the symmetry within a dark-field is increased or when the symmetry between the patterns for \mathbf{G} and $-\mathbf{G}$ is increased.

TABLE 2. PATTERN SYMMETRIES

(Where a dash appears in column 7, the special symmetries can be deduced from columns 5 and 6 of this table (or from table 1).)

diffraction group	bright field	whole pattern	dark field		$\pm \mathbf{G}$		projection diffraction group
			general	special	general	special	
1	1	1	1	none	1	none	1 _R
1 _R	2	1	2	none	1	none	
2	2	2	1	none	2	none	21 _R
2 _R	1	1	1	none	2 _R	none	
21 _R	2	2	2	none	21 _R	none	
m _R	m	1	1	m	1	m _R	m1 _R
m	m	m	1	m	1	m	
m1 _R	2mm	m	2	2mm	1	m1 _R	
2m _R m _R	2mm	2	1	m	2	—	2mm1 _R
2mm	2mm	2mm	1	m	2	—	
2 _R mm _R	m	m	1	m	2 _R	—	
2mm1 _R	2mm	2mm	2	2mm	21 _R	—	
4	4	4	1	none	2	none	41 _R
4 _R	4	2	1	none	2	none	
41 _R	4	4	2	none	21 _R	none	
4m _R m _R	4mm	4	1	m	2	—	4mm1 _R
4mm	4mm	4mm	1	m	2	—	
4 _R mm _R	4mm	2mm	1	m	2	—	
4mm1 _R	4mm	4mm	2	2mm	21 _R	—	
3	3	3	1	none	1	none	31 _R
31 _R	6	3	2	none	1	none	
3m _R	3m	3	1	m	1	m _R	3m1 _R
3m	3m	3m	1	m	1	m	
3m1 _R	6mm	3m	2	2mm	1	m1 _R	
6	6	6	1	none	2	none	61 _R
6 _R	3	3	1	none	2 _R	none	
61 _R	6	6	2	none	21 _R	none	
6m _R m _R	6mm	6	1	m	2	—	6mm1 _R
6mm	6mm	6mm	1	m	2	—	
6 _R mm _R	3m	3m	1	m	2 _R	—	
6mm1 _R	6mm	6mm	2	2mm	21 _R	—	

Table 2 lists the diffraction groups and gives information on the special cases for each one. The second column gives the two dimensional point group symmetry of the bright field image (either bend-contour or convergent-beam image) while the third gives that of the whole pattern. The whole-pattern symmetry is the two dimensional point-group symmetry of the patterns given in table 1; this is useful because a single convergent beam pattern (taken symmetrically about the zone axis and including dark-field orders) has this symmetry (the dark-field images are off

centre and lie in a region wholly outside the centres of their internal symmetry); several exposures may be required to reveal the full diffraction symmetry. The next two columns of table 2 give the symmetry within each dark field order: the first gives the presence or absence of the internal twofold axis (this is obvious from table 1 but it is convenient to bring it together with the other information in this table), the second gives the internal symmetry of dark-field images corresponding to images formed in reflexions parallel to some or all of the radial lines of table 1. The next two columns of the table give the symmetry relation between the dark-field images using reflexions \mathbf{G} and $-\mathbf{G}$; the first of the two columns gives the general relation (which may be observed directly from table 1), while the second gives the additional relations which apply when \mathbf{G} is parallel to some or all of the radial lines in table 1. These relations between \mathbf{G} and $-\mathbf{G}$ dark-field images are given by using the appropriate diffraction group symbols. The diagrams corresponding to 2 , 2_R and 21_R are the same as those in table 1, diagrams for m , m_R and $m1_R$ are given in figure 10 since they are slightly different from the corresponding diagrams in table 1 where the dark-field orders are not $\pm \mathbf{G}$, but only mirror related.

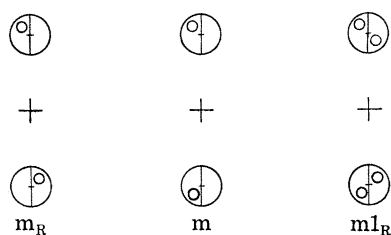


FIGURE 10. Diagrams which represent certain relations in the special case when they refer to dark-field images for $\pm \mathbf{G}$; these relations in the general case are given in table 1.

The value of tabulating the particular relations in table 2 is that experimentally, especially where bend contours rather than convergent beam patterns are observed, it is frequently easy to establish the internal symmetry of bright- and dark-field orders and the relation between $\pm \mathbf{G}$ images and hence determine the diffraction group whereas it would be laborious and difficult to explore the full symmetry relations of a general dark-field order.

In table 3 the interrelation between the specimen point group and the diffraction groups is given. This table may be used to determine the crystal point group from observation of zone axis patterns; it also shows which diffraction groups arise from each point group but that is more conveniently obtained from table 4. The latter lists, against each point group, the diffraction groups to which it can give rise and the zone axis directions which produce them.

When the projection approximation is valid the specimen behaves as though it has only two dimensional periodicity. It therefore must contain a horizontal mirror (cf. § 2 (*d*)). Examination of specific cases reveals that no further symmetry elements are introduced, except accidentally. If we now consider how this symmetry change effects the results of tables 1–4 we find that the 31 diffraction groups are reduced to the ten projection diffraction groups (§ 2 (*d*)). The relation of the latter to the diffraction groups is somewhat analogous to the relation between the Laue groups and the three dimensional point groups in X-ray work. The way in which the diffraction groups and projection diffraction groups are related is given in table 2; this reveals the reason for the grouping of the items in tables 1 and 2.

In this case it is possible to derive the point group of the crystal (except for the previously mentioned ambiguity between 4 and $\bar{4}$: § 2 (*d*)) by determining the projection diffraction group

ELECTRON DIFFRACTION SYMMETRIES

189

TABLE 4. ZONE AXIS SYMMETRIES

point group	$\langle 111 \rangle$	$\langle 100 \rangle$	$\langle 110 \rangle$	$\langle uvo \rangle$	$\langle uuv \rangle$	$[uvw]$	
m3m	$6_R mm_R$	$4 mm 1_R$	$2 mm 1_R$	$2_R mm_R$	$2_R mm_R$	2_R	
43m	$3m$	$4_R mm_R$	$m 1_R$	m_R	m	1	
432	$3m_R$	$4m_R m_R$	$2m_R m_R$	m_R	m_R	1	
point group	$\langle 111 \rangle$	$\langle 100 \rangle$		$\langle uvo \rangle$	$[uvw]$		
m3	6_R	$2 mm 1_R$		$2_R mm_R$	2_R		
23	3	$2m_R m_R$		m_R	1		
point group	$[0001]$	$\langle 11\bar{2}0 \rangle$	$\langle 1\bar{1}00 \rangle$	$[uv.o]$	$[uu.w]$	$[u\bar{u}.w]$	$[uv.w]$
$6/mmm$	$6 mm 1_R$	$2 mm 1_R$	$2 mm 1_R$	$2_R mm_R$	$2_R mm_R$	$2_R mm_R$	2_R
$\bar{6}m2$	$3m 1_R$	$m 1_R$	$2mm$	m	m_R	m	1
$6mm$	$6mm$	$m 1_R$	$m 1_R$	m_R	m	m	1
622	$6m_R m_R$	$2m_R m_R$	$2m_R m_R$	m_R	m_R	m_R	1
point group		$[0001]$		$[uv.o]$		$[uv.w]$	
$6/m$		$6 1_R$		$2_R mm_R$		2_R	
$\bar{6}$		$3 1_R$		m		1	
6		6		m_R		1	
point group	$[0001]$		$\langle 11\bar{2}0 \rangle$		$[u\bar{u}.w]$		$[uv.w]$
$\bar{3}m$	$6_R mm_R$		$2 1_R$		$2_R mm_R$		2_R
$3m$	$3m$		1_R		m		1
32	$3m_R$		2		m_R		1
point group		$[0001]$				$[uv.w]$	
$\bar{3}$		6_R				2_R	
3		3				1	
point group	$[001]$	$\langle 100 \rangle$	$\langle 110 \rangle$	$[uow]$	$[uvo]$	$[uuv]$	$[uvw]$
$4/mmm$	$4 mm 1_R$	$2 mm 1_R$	$2 mm 1_R$	$2_R mm_R$	$2_R mm_R$	$2_R mm_R$	2_R
$42m$	$4_R mm_R$	$2m_R m_R$	$m 1_R$	m_R	m_R	m	1
$4mm$	$4mm$	$m 1_R$	$m 1_R$	m	m_R	m	1
422	$4m_R m_R$	$2m_R m_R$	$2m_R m_R$	m_R	m_R	m_R	1
point group		$[001]$		$[uvo]$		$[uvw]$	
$4/m$		$4 1_R$		$2_R mm_R$		2_R	
$\bar{4}$		4_R		m_R		1	
4		4		m_R		1	
point group	$[001]$	$\langle 100 \rangle$		$[uow]$	$[uvo]$	$[uvw]$	
mmm	$2 mm 1_R$	$2 mm 1_R$		$2_R mm_R$	$2_R mm_R$	2_R	
$mm2$	$2mm$	$m 1_R$		m	m_R	1	
222	$2m_R m_R$	$2m_R m_R$		m_R	m_R	1	
point group		$[010]$		$[uow]$		$[uvw]$	
$2/m$		$2 1_R$		$2_R mm_R$		2_R	
m		1_R		m		1	
2		2		m_R		1	
point group					$[uvw]$		
$\bar{1}$					2_R		
1					1		

5. EXPERIMENTAL RESULTS

The results derived and tabulated in the previous sections may be applied to either convergent beam or bend contour patterns. However, there are a number of ways in which the experiments deviate from the simplicity of the model assumed in §2. The normal to the specimen may not coincide with the zone axis; inelastically or diffusely scattered electrons may contribute to the patterns and the specimens may have complicated shapes. In addition, when working with bend contour patterns, allowance must generally be made for irregularities in the specimen curvature. Although this might seem to be a serious handicap to contour work we have found that it is possible to detect quite subtle differences of symmetry by relying on the large angular view in contour patterns and the eye's ability at pattern recognition.

The question of the visibility of pattern features which distinguish the various point groups has not so far been raised. We now intend to examine this point by experimental results obtained from convergent beam work on specimens of GaAs and Ge. This is a sensitive test because the crystal potential of GaAs is very similar to that of Ge, but has a small antisymmetric part. The specimens were prepared from carefully oriented sections of bulk material by ion or chemical etching and had wedge angles which were generally less than 10° .

In order to decide which tables to refer to it is necessary to ascertain whether upper layer effects are playing a significant rôle in the pattern symmetries. In the case of thick specimens the small angular width of the upper layer lines generally makes it a simple matter to arrive at a firm conclusion. In thin crystals the upper layer effects often take the form of broad spots which are similar to the spot patterns arising from zero layer interactions. To discover the origin of these spots it is necessary to change the microscope operating voltage by approximately 5 kV (a larger change in voltage might alter the zero layer diffraction). If the pattern is scarcely affected by such small voltage changes then upper layer effects are unimportant.

A study of table 2 makes it clear that it is profitable, when trying to identify the point group of a crystalline specimen to look at zone axes of high symmetry. There are just four cases where a unique conclusion may be drawn from one zone axis convergent beam pattern. For example, there are seven different pattern symmetries for fourfold axes and in one case (4_R) it is only necessary to inspect the whole pattern and bright field symmetries to identify uniquely the crystal point group. In two further cases ($4m_Rm_R$, 4_Rmm_R) it is only necessary to distinguish a cubic from a tetragonal crystal to complete the identification. The 4 and 41_R patterns may be distinguished by the internal symmetry of any one dark-field pattern. A table, which facilitates the systematic use of patterns in this way, for all the diffraction groups has been given by Buxton & Eades (1976). The $\langle 100 \rangle$ pattern of GaAs (point group $\bar{4}3m$) has only $2mm$ whole pattern symmetry and it may, therefore, be distinguished from the Ge (point group $m\bar{3}m$) pattern. This result is clearly displayed by the four $\{020\}$ disks in figure 11, plate 1. Although there is no question about the symmetry of this pattern it should be pointed out that the specimen thickness had to be carefully chosen. For very thin specimens ($\lesssim 40$ nm) there was insufficient detail in the $\{020\}$ disks to decide the pattern symmetry, while for very thick specimens ($\gtrsim 200$ nm) the $\{020\}$ disks became invisible against the diffuse background, changing the symmetry to $4mm$. The thickness dependence of this result is apparently a consequence of the weak $\{020\}$ reflexion in GaAs since the pattern from a thick specimen of InP (figure 12, plate 1) retains $2mm$ symmetry.

For hexagonal and trigonal crystals it is most valuable to study the $[0001]$ patterns. Each

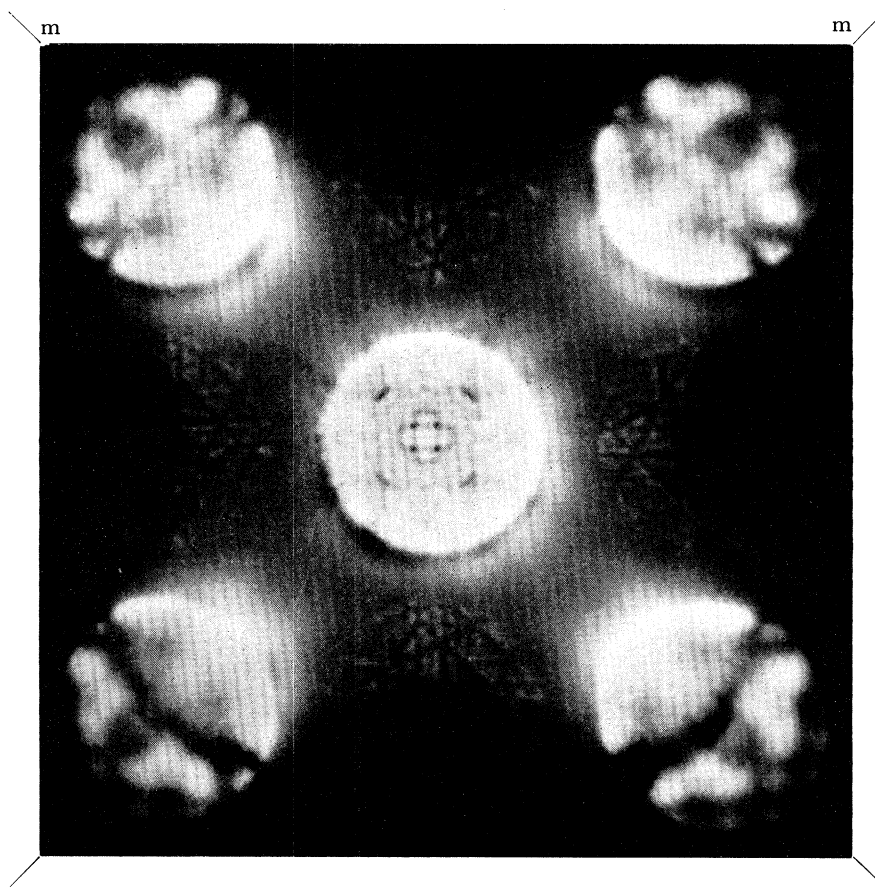


FIGURE 11. GaAs $\langle 100 \rangle$ axial convergent beam pattern from a $\{100\}$ foil; the micrograph was taken at a nominal operating voltage of 60 kV with the specimen cooled to a temperature of approximately 90 K. $\{020\}$ disks are rather weak and adjoin the central disk. In this and subsequent figures any discrepancy between the pattern and disk centres is due to slight misalignment of the crystal.

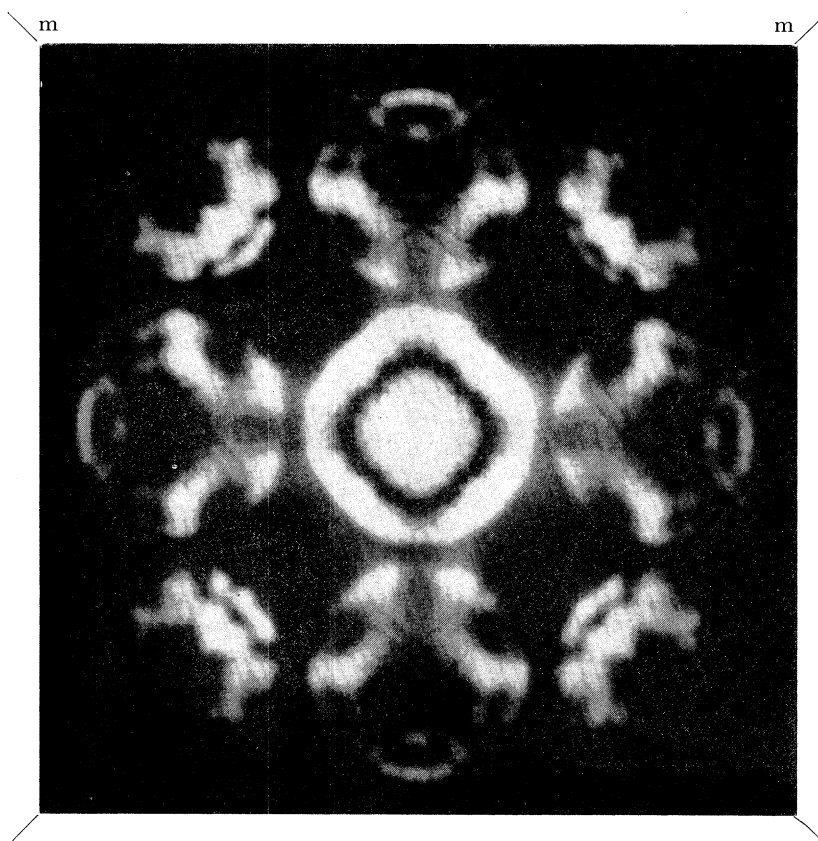


FIGURE 12. InP $\langle 100 \rangle$ axial convergent beam pattern from a $\{100\}$ foil; the micrograph was taken at a nominal operating voltage of 80 kV with the specimen cooled to a temperature of approximately 90 K. The $\{020\}$ disks lie closest to the central disk.

(Facing p. 190)

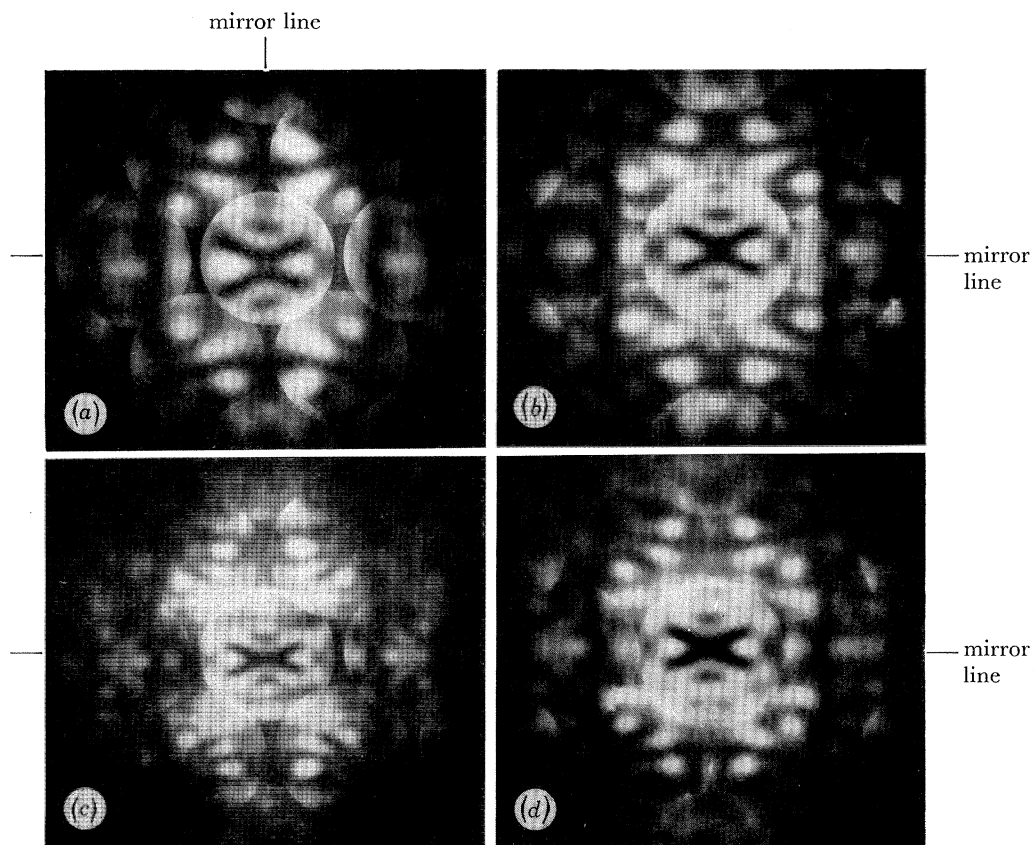


FIGURE 13. $\langle 110 \rangle$ axial convergent beam patterns of Ge and GaAs taken at 100 kV. (a) and (c) are from Ge $\{111\}$ foils of different thickness; (b) and (d) are from GaAs $\{110\}$ foils of approximately the same thickness as used in (a) and (c). The $\pm \{002\}$ disks lie on the horizontal lines either side of the central disk. The central disk of (a) is probably distorted by thickness change within the illuminated area of the specimen.

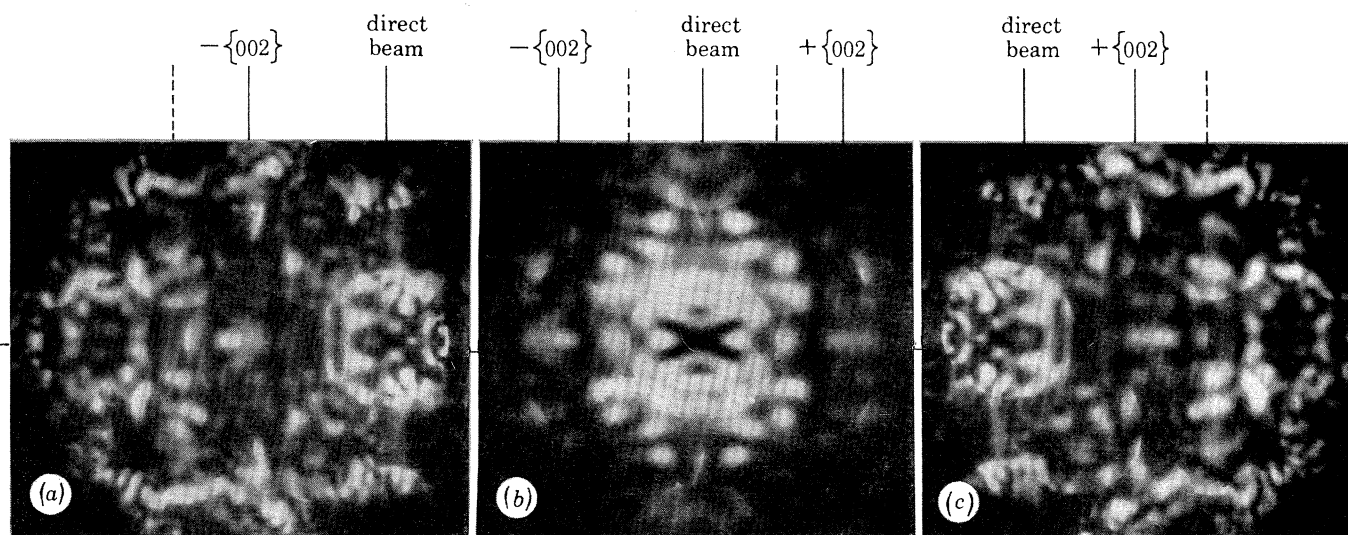


FIGURE 14. GaAs $\langle 110 \rangle$ convergent beam patterns from a $\{110\}$ foil taken at an operating voltage of 100 kV. There is axial illumination in (b); in (a) and (c) the image of the aperture has been shifted to the right and left respectively. The centres of the zero order and $\pm \{002\}$ disks are marked by the intersection of the solid vertical lines with the horizontal line. The dashed lines intersect the horizontal line at the $\pm \{002\}$ Bragg positions.

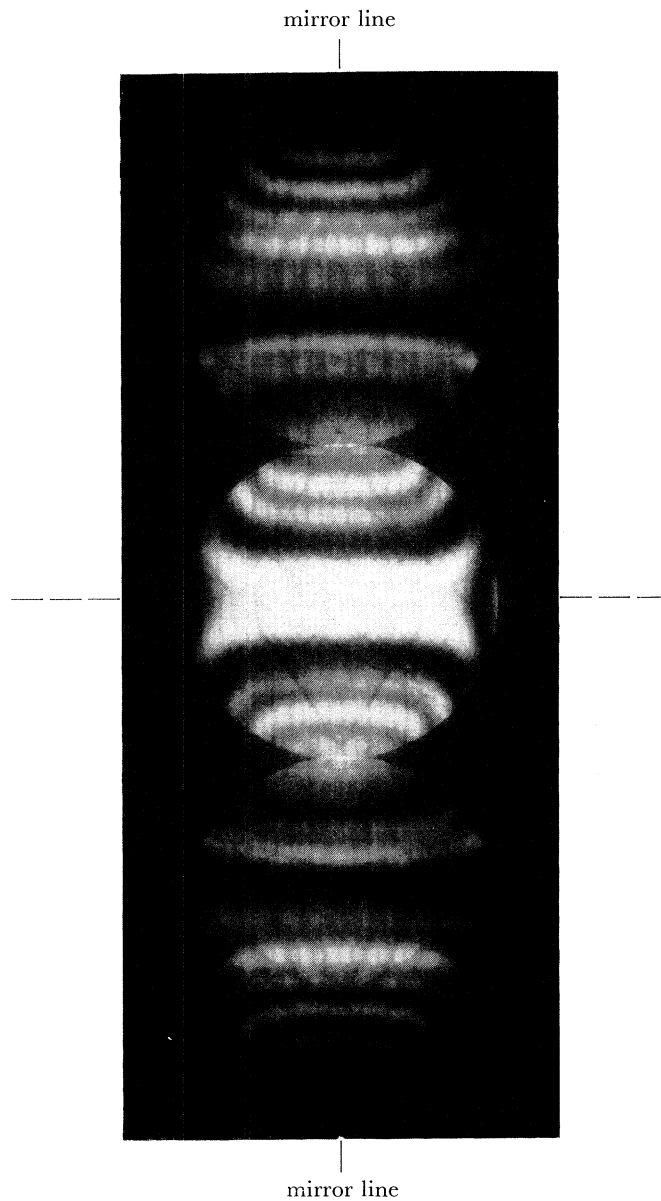


FIGURE 15. Si $\langle 211 \rangle$ axial convergent beam pattern from a $\{111\}$ foil taken at an operating voltage of approximately 96.5 kV. The broken horizontal line would be a mirror line in the projection approximation.

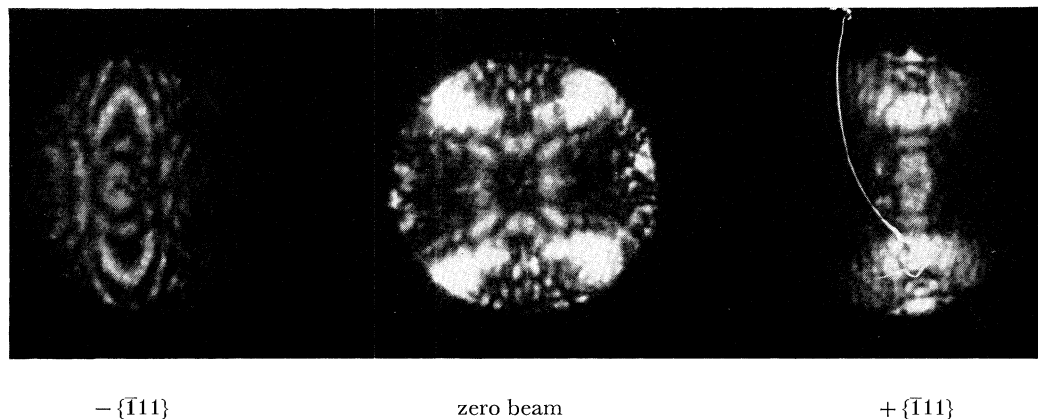


FIGURE 16. Multiple dark-field image of gold $\langle 211 \rangle$ showing out-of-focus bend contours in each disk. The $\{111\}$ specimen has been tilted through 20° about the $\langle 0\bar{1}1 \rangle$ direction perpendicular to the line of the disks to obtain this pattern. Tables 4 and 2 predict 2 mm symmetry for the pattern but the tilted surfaces destroy the mirror line parallel to the tilt axis (M. D. Shannon, unpublished work).

hexagonal point group has a unique [0001] pattern symmetry, while the symmetry of each trigonal [0001] pattern is shared with the $\langle 111 \rangle$ axis of just one cubic point group. The GaAs and Ge $\langle 111 \rangle$ patterns are particularly hard to distinguish. It is necessary to perform experiments revealing the internal or relative symmetries of dark-field orders; these experiments are comparatively difficult and do not yield really convincing results. The difficulty arises from the need to maintain the same specimen thickness whilst changing the angle of incidence with respect to the zone axis. On account of the relatively large reciprocal lattice vectors normal to $\langle 111 \rangle$ it is not practical to change the specimen inclination without displacing the probe significantly and we therefore achieved the required effect by displacing the second condenser aperture. For large displacements this procedure also fails because the aberrations both increase the spot size and cause distortion in the back focal plane. However, the difference between the six $\{2\bar{2}0\}$ reflexions of Ge and GaAs is the presence of an internal mirror line and to observe this it is only necessary to carry out a relatively small aperture displacement. Unfortunately, the difference between the patterns obtained in this way amounts to a small change in the relative intensity of upper layer lines in GaAs either side of the position of the mirror line in Ge. Moreover some doubt is thrown even onto these results by the observation of a similar asymmetry for thick Ge specimens. This is apparently due to the displacement between the peak of diffuse scattering, which is centred on the mean beam direction, and the centre of the dark field disk.

So far our experiments have relied on upper layer effects to distinguish the GaAs from the Ge. It is, however, also possible to detect the difference between these two materials in the projection approximation. One of the most useful zone axes in drawing the distinction is the $\langle 110 \rangle$ axis. According to tables 4 and 1, the whole pattern symmetry of GaAs is m whereas that of Ge is $2mm$; the lower symmetry of the former is revealed by the difference between the $\pm\{002\}$ disks (figure 13, plate 2). As an example of the determination of the internal symmetry of a dark-field order, we show in figure 14 convergent beam patterns of GaAs obtained by displacing the condenser aperture to tilt the illumination to $\pm\{002\}$. These reveal the predicted $2mm$ symmetry in the $\{002\}$ disks. Note that in this case the pattern symmetry is not affected by making the projection approximation.

Finally, an example of a lower symmetry zone axis displays the usefulness of being able to distinguish upper and zero layer effects (figure 15). The symmetries of both the whole pattern and of the bright field are m , but if we ignore the fine lines and so effectively use the projection approximation, the symmetries are both $2mm$. The only diffraction group with this property is 2_Rmm_R , the predicted symmetry for Si $\langle 211 \rangle$.

We have so far presented results where the zone axis is approximately parallel to the surface normal as assumed in the earlier sections. However it is common to tilt through angles of 30° or more in crystallographic work with the electron microscope. Our experience of such experiments is that the bright field symmetry is hardly affected (but see § 6). Even in the case of a Si $\{100\}$ section tilted to $\langle 111 \rangle$ the only effect was a small change in the relative visibility of equivalent upper layer lines. The situation has, however, been found to be much more complicated when dark field symmetries are studied. In some cases tilts of 20° or less have a marked effect on these patterns as in the example illustrated in figure 16 for a gold $\{111\}$ epitaxial film tilted to $\langle 211 \rangle$. In others, the patterns are relatively insensitive to tilt. Further work is required to clarify this.

6. DISCUSSION AND CONCLUSIONS

As we have used only a very specialized model for the scattering processes, it is worth noting some of the deficiencies and advantages of our approach. We have not discussed inelastic or diffuse scattering of the incident electrons, except in so far as these processes absorb intensity from the coherent elastically scattered waves. Also we have yet to investigate the detailed effect of the shape of the specimen (Moodie 1972) but it seems that where shape effects are important, the diffraction symmetry may not be one of the diffraction groups. However, if the specimen is a platelet, the diffraction groups do describe *all* the possible symmetry properties of the diffracted waves. For this type of specimen the exact orientation of the surfaces is important (Goodman 1974), and the diffraction group observed may well be different from that predicted in table 4 if the symmetric Laue condition is not satisfied (e.g. figure 16). In this case the diffraction group cannot be obtained from the crystal point group alone. It should be obtained from the space group of the platelet itself.

The specimens usually used in microscopy are chemically or ion thinned, and have very uneven surfaces, often forming a rough wedge shape. Although the experiments discussed in § 5 were performed on this type of specimen, we have seen that the results agree with our predictions, which essentially depend on three assumptions: (1) the symmetric Laue condition; (2) flat surfaces; (3) that irreducible lattice translations normal to the surfaces assumed in (2) are not important.

In the absence of perfectly flat surfaces it seems that assumptions (1) and (3) will not be important, and that the roughness itself will only contribute to background noise in our pictures. Also, for the relatively thick specimens we have used, much of the image contrast is probably due to inelastically scattered electrons which remain partially coherent with the elastically scattered electrons (Howie 1963). The details of the surfaces would not be important for these electrons. However, for thin specimens with flat surfaces, irreducible lattice translations not parallel to the surface may be important and the diffraction group must then be derived from the space group of the specimen itself. This space group will be one of the 80 diaperiodic space groups (Megaw 1973 and cf. § 2 (b)).

One important advantage of our model has been that it treated the scattering dynamically, without any restrictions on the number or origin of the diffracted waves. Upper-layer effects were included naturally within the scheme, although it was easy to discuss the effect of the projection approximation and systematic diffraction. The Bloch wave approach (see, for example, Hirsch *et al.* 1965) was not used because it becomes complicated if upper layer effects are important. The complications arise from the choice of the linearly independent Bloch waves and the boundary conditions at the surfaces (Dederichs 1971). If the projection approximation is valid, and elastically back scattered electrons are ignored, the Bloch wave expansion of the electron wavefunction in the crystal slab is quite simple (Hirsch *et al.* 1965) and can be used to derive the symmetry properties in a straightforward way (some examples are discussed by Fukuhara 1966). We have checked that our results may be obtained from the Bloch wave approach. Interestingly, absorption can be included exactly in the Bloch wave theory (Dederichs 1971) and like the present approach it can be extended to non-local optical potentials. No new results are obtained.

Although our method describes the diffraction exactly, it does not provide explicit solutions for the transmission coefficients $T_{\mathcal{G}}^{(+)}(\mathbf{K})$. We have therefore not discussed forbidden or dynamically forbidden reflections (Gjønnes & Moodie 1965) which can themselves provide

useful symmetry information about the space group. We have obtained a set of simple rules which can often be applied quickly and easily to enable the crystal point group of the specimen to be determined. It is significant that the inversion centre has no privileged position in this scheme since Friedel's law does not apply to electron diffraction. We have also shown that high resolution lattice images can contribute to the determination of the crystal point group and space group.

Despite the limitations discussed here, we have shown how the convergent beam and bend contour techniques facilitate the determination of crystal symmetries.

We wish to acknowledge the enthusiastic support and encouragement of this work by Professor F. C. Frank, F.R.S., and the assistance of the Royal Radar Establishment, Malvern in providing specimens of gallium arsenide and indium phosphide. I.C.I., under their newly created Joint Research Scheme, supported this work, in particular through a Research Associateship (J.A.E.). The Science Research Council also provided support in the form of a Postdoctoral Research Fellowship (B.F.B.) and a C.A.S.E. Research Studentship with the R.R.E. (G.M.R.)

REFERENCES

- Bilhorn, D. E., Foldy, L. L., Thaler, R. M., Tobocman, W. & Madsen, V. A. 1964 *J. Math. Phys.* **5**, 435–441.
 Berry, M. V. 1971 *J. Phys. C* **4**, 697–722.
 Buerger, M. J. 1960 *Crystal structure analysis*, pp. 283–301. New York: Wiley.
 Buxton, B. F. & Eades, J. A. 1976 In *Developments in electron microscopy and analysis* (ed. J. A. Venables). London: Academic Press.
 Cowley, J. M. 1967 *Prog. mat. Sci.* **13**, 267–321.
 Dederichs, P. H. 1971 *Dynamical diffraction theory*, KFA-JUL-Report, JUL-797-FF 1971.
 Dederichs, P. H. 1972 *Solid State Phys.* **27**, 135–326.
 Fukuhara, A. 1966 *J. Phys. Soc., Japan* **21**, 2645–2662.
 Fujiwara, K. 1961 *J. Phys. Soc., Japan* **16**, 2226–2238.
 Fujiwara, K. 1962 *J. Phys. Soc., Japan* **17** (Suppl. B II), 118–123.
 Gjønnes, J. & Moodie, A. F. 1965 *Acta Cryst.* **19**, 65–67.
 Goodman, P. 1974 *Nature, Lond.* **251**, 698–701.
 Goodman, P. & Lempfuhr, G. 1968 *Acta Cryst. A* **24**, 339–347.
 Goodman, P. & Steeds, J. W. 1975 Submitted to *Nature, Lond.*
 Hirsch, P. B., Howie, A., Nicholson, R. B., Pashley, D. W. & Whelan, M. J. 1965 *Electron microscopy of thin crystals*, pp. 208–221, 276–294. London: Butterworths.
 Howie, A. 1963 *Proc. R. Soc. Lond. A* **271**, 268–287.
 Howie, A. 1966 *Phil. Mag.* **14**, 223–287.
 Howie, A. & Stern, R. M. 1972 *Z. Naturforsch.* **27a**, 382–389.
 Iijima, S. 1971 *J. appl. Phys.* **42**, 5891–5893.
 International Tables for X-Ray Crystallography 1965 Vol. 1, pp. 38–39. Birmingham: Kynoch Press.
 Joy, D. 1974 In *Quantitative scanning electron microscopy* (ed. D. B. Holt, M. D. Muir, P. R. Grant & I. M. Boswarva), pp. 131–182. London: Academic Press.
 Kambe, K. 1967 *Z. Naturforsch.* **22a**, 422–431.
 Lenz, F. A. 1971 In *Electron microscopy in material science* (ed. U. Valdre), pp. 539–569. London: Academic Press.
 Megaw, H. D. 1973 *Crystal structures: a working approach*, pp. 177–184. London: Saunders.
 Moodie, A. F. 1972 *Z. Naturforsch.* **27a**, 437–440.
 Pogany, A. P. & Turner, P. S. 1968 *Acta Cryst. A* **24**, 103–109.
 Rackham, G. M., Jones, P. M. & Steeds, J. W. 1974 *Eighth International Congress on Electron Microscopy*, vol. 1, p. 336 and p. 355. Canberra: Australian Academy of Science.
 Seitz, F. 1936 *Ann. Math.* **37**, 17–28.
 Shubnikov, A. V. 1964 *Coloured symmetry*. New York: Pergamon Press, Inc.
 Steeds, J. W. 1974 In *Diffraction studies of real atoms and real crystals*, pp. 310–311. Canberra: Australian Academy of Science.
 Steeds, J. W., Tatlock, G. J. & Hampson, J. 1973 *Nature, Lond.* **241**, 435–439.
 Tanaka, M. 1975 *Acta Cryst. A* **31**, 59–63.

- Tanaka, M. & Honjo, G. 1964 *J. Phys. Soc., Japan* **19**, 954–970.
- Thomas, G. 1970 In *Modern diffraction and imaging techniques in material science* (ed. S. Amelinckx, R. Gevers, G. Remaut & J. Van Landuyt), pp. 159–185. Amsterdam: North Holland.
- Tournarie, M. 1961 *C. r. hebd. Séanc. Acad. Sci., Paris* **252**, 2862–2864.
- Tournarie, M. 1962 *J. Phys. Soc., Japan* **17** (Suppl. B II), 98–100.
- Uyeda, R. 1974 *J. appl. Cryst.* **7**, 1–18.
- Zachariasen, W. H. 1945 *Theory of X-ray diffraction in crystals*, pp. 24–81. New York: Dover.

m

m

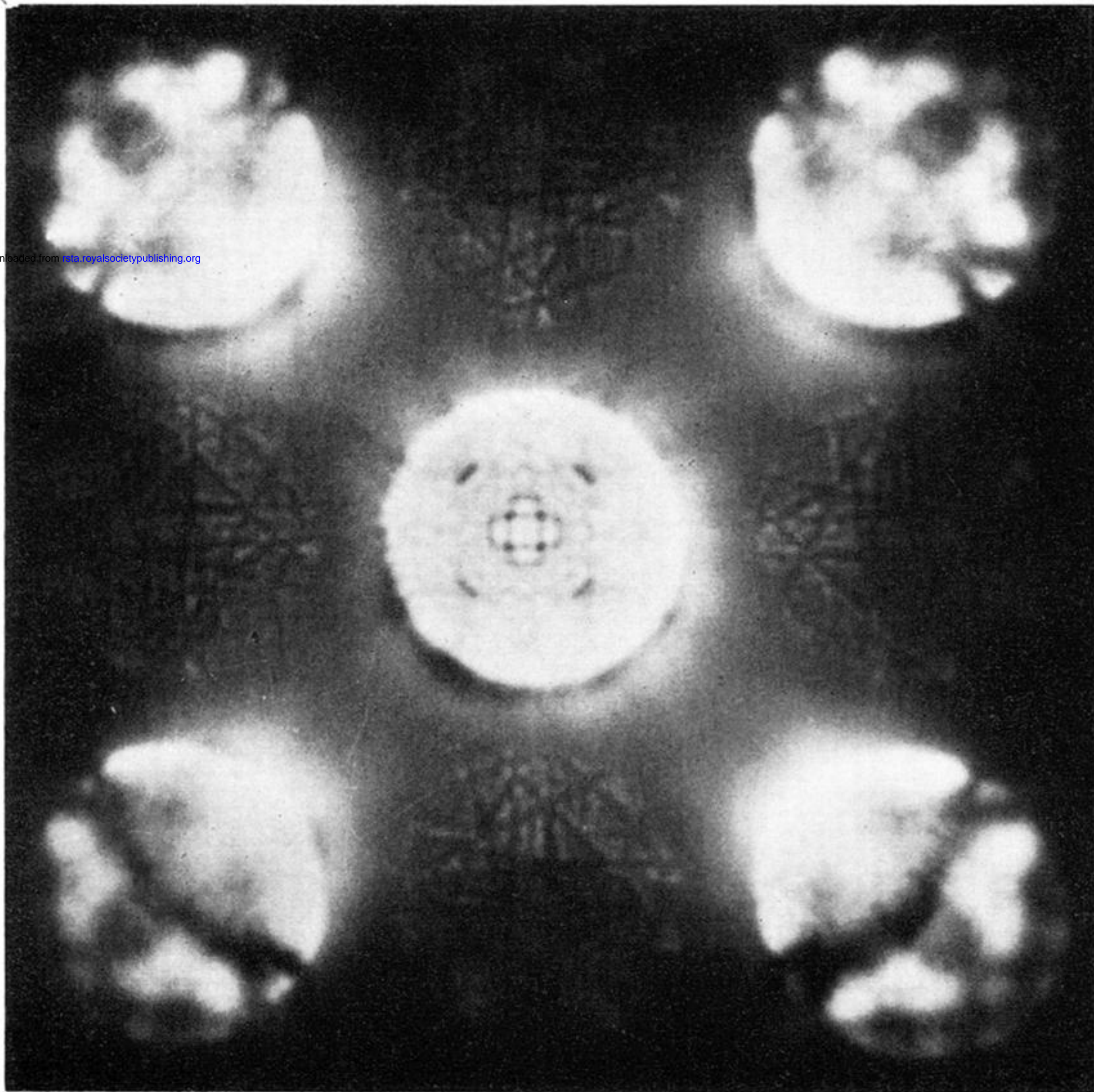
Downloaded from rsta.royalsocietypublishing.org

FIGURE 11. GaAs $\langle 100 \rangle$ axial convergent beam pattern from a $\{100\}$ foil; the micrograph was taken at a nominal operating voltage of 60 kV with the specimen cooled to a temperature of approximately 90 K. $\{020\}$ disks are rather weak and adjoin the central disk. In this and subsequent figures any discrepancy between the pattern and disk centres is due to slight misalignment of the crystal.

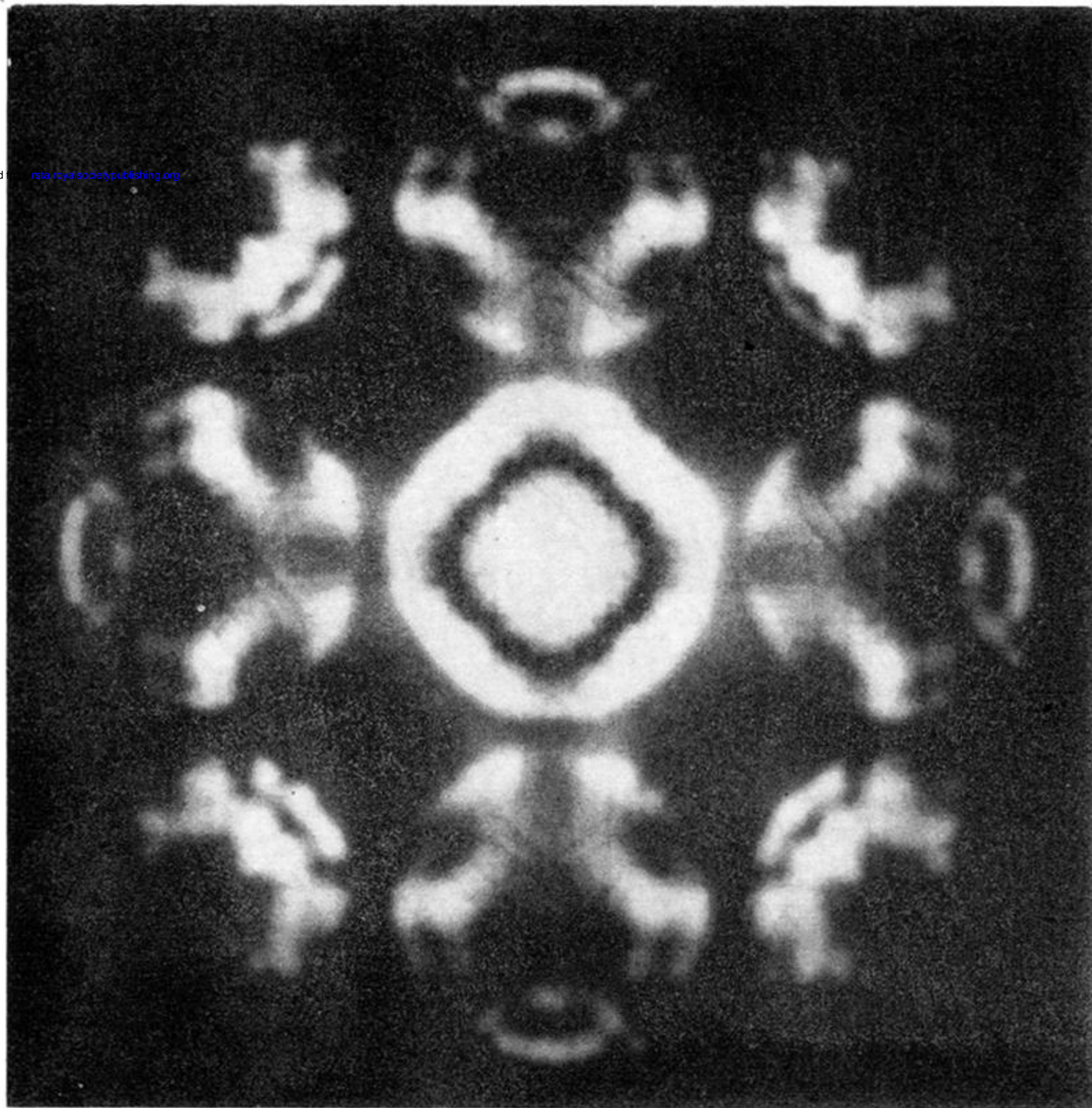


FIGURE 12. InP $\langle 100 \rangle$ axial convergent beam pattern from a $\{100\}$ foil; the micrograph was taken at a nominal operating voltage of 80 kV with the specimen cooled to a temperature of approximately 90 K. The $\{020\}$ disks lie closest to the central disk.

mirror line

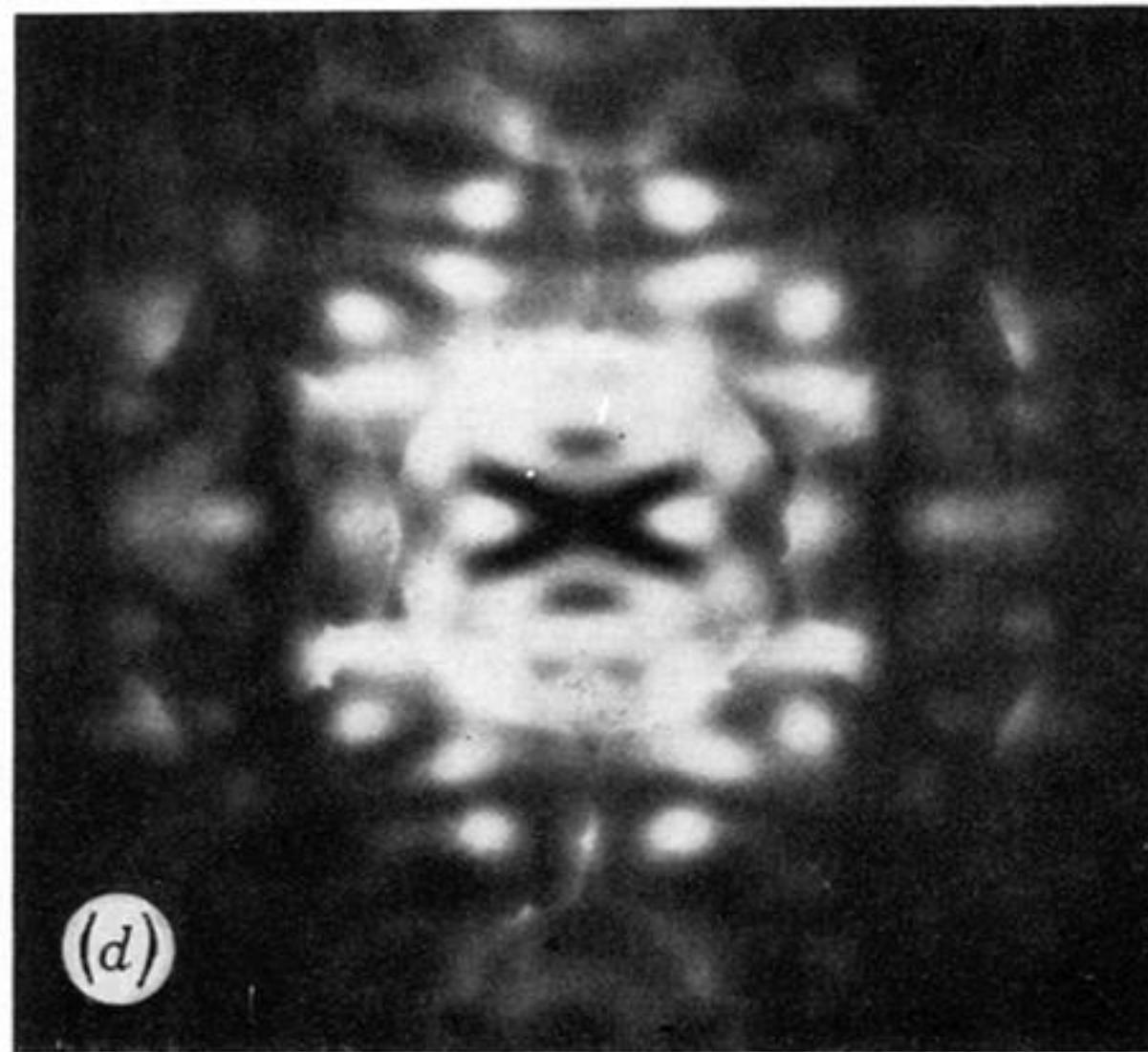
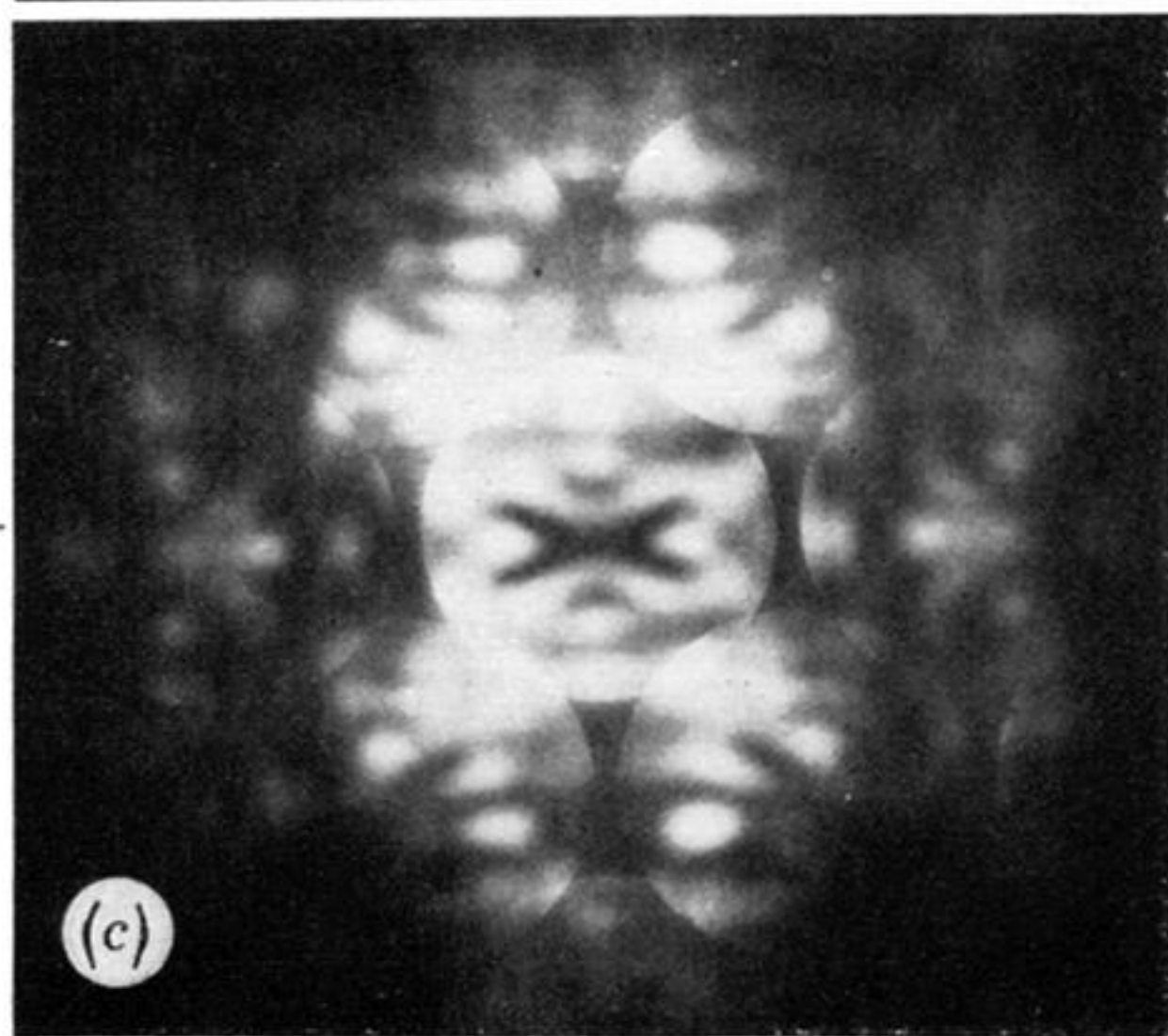
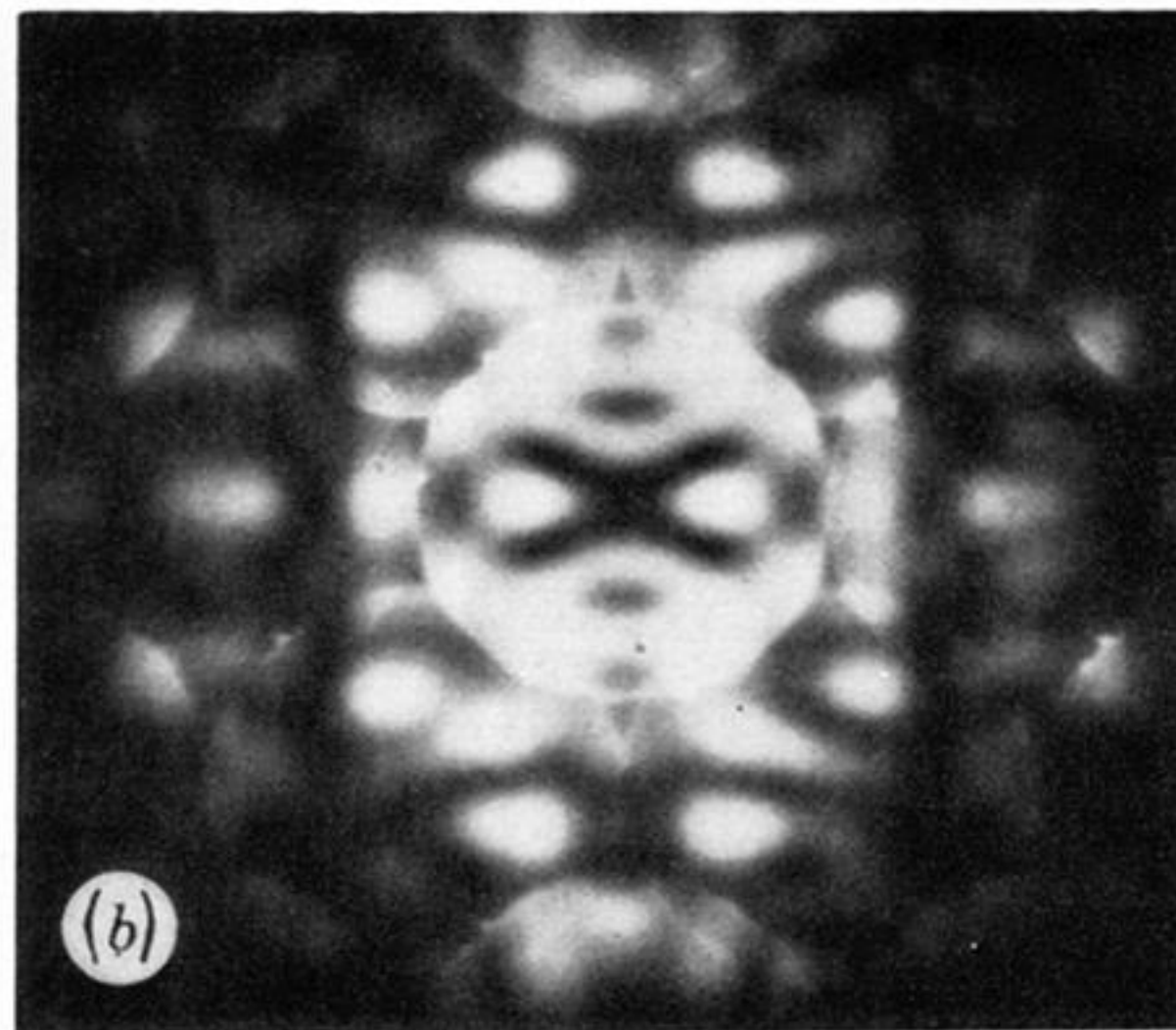
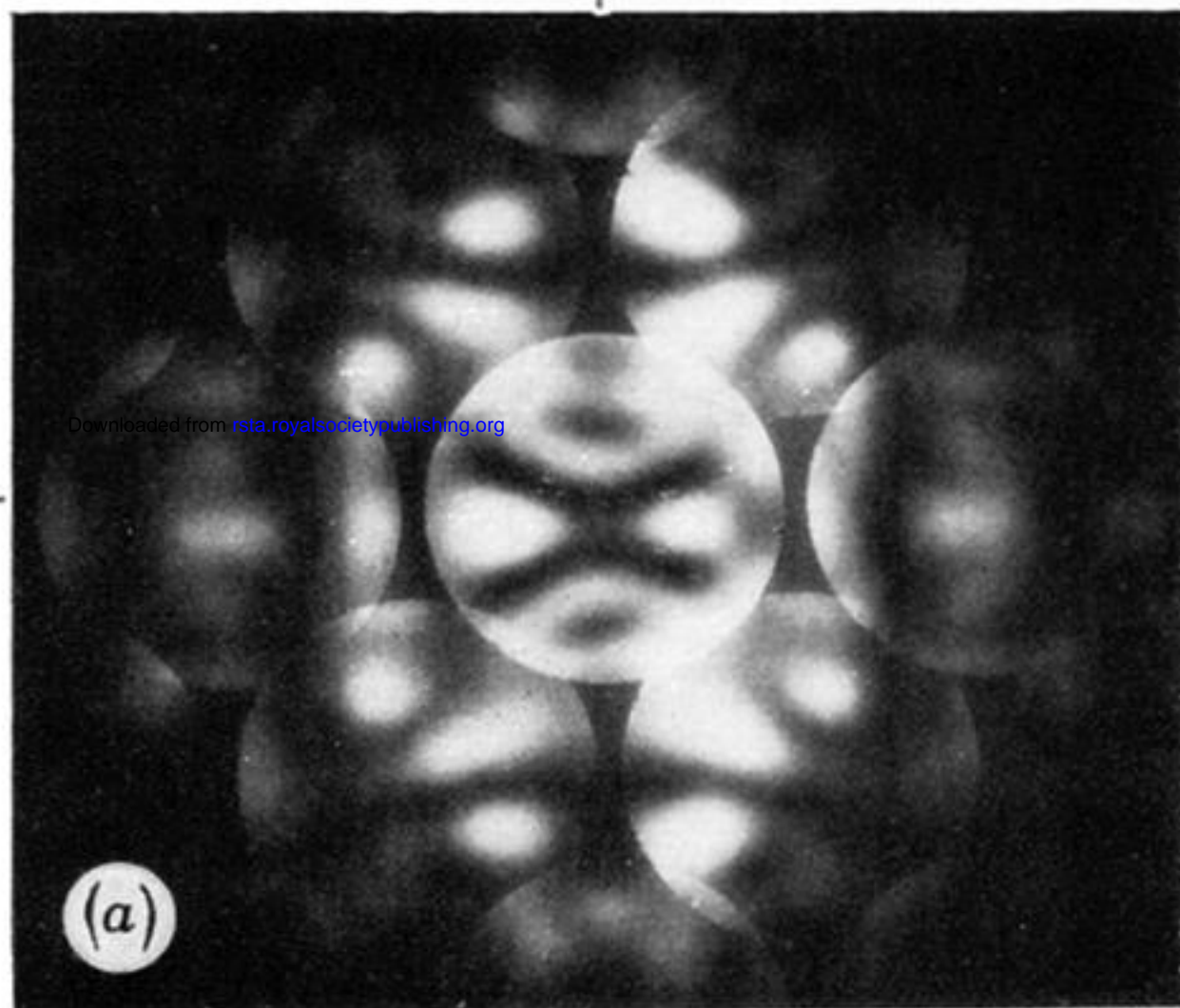


FIGURE 13. $\langle 110 \rangle$ axial convergent beam patterns of Ge and GaAs taken at 100 kV. (a) and (c) are from Ge $\{111\}$ foils of different thickness; (b) and (d) are from GaAs $\{110\}$ foils of approximately the same thickness as used in (a) and (c). The $\pm \{002\}$ disks lie on the horizontal lines either side of the central disk. The central disk of (a) is probably distorted by thickness change within the illuminated area of the specimen.

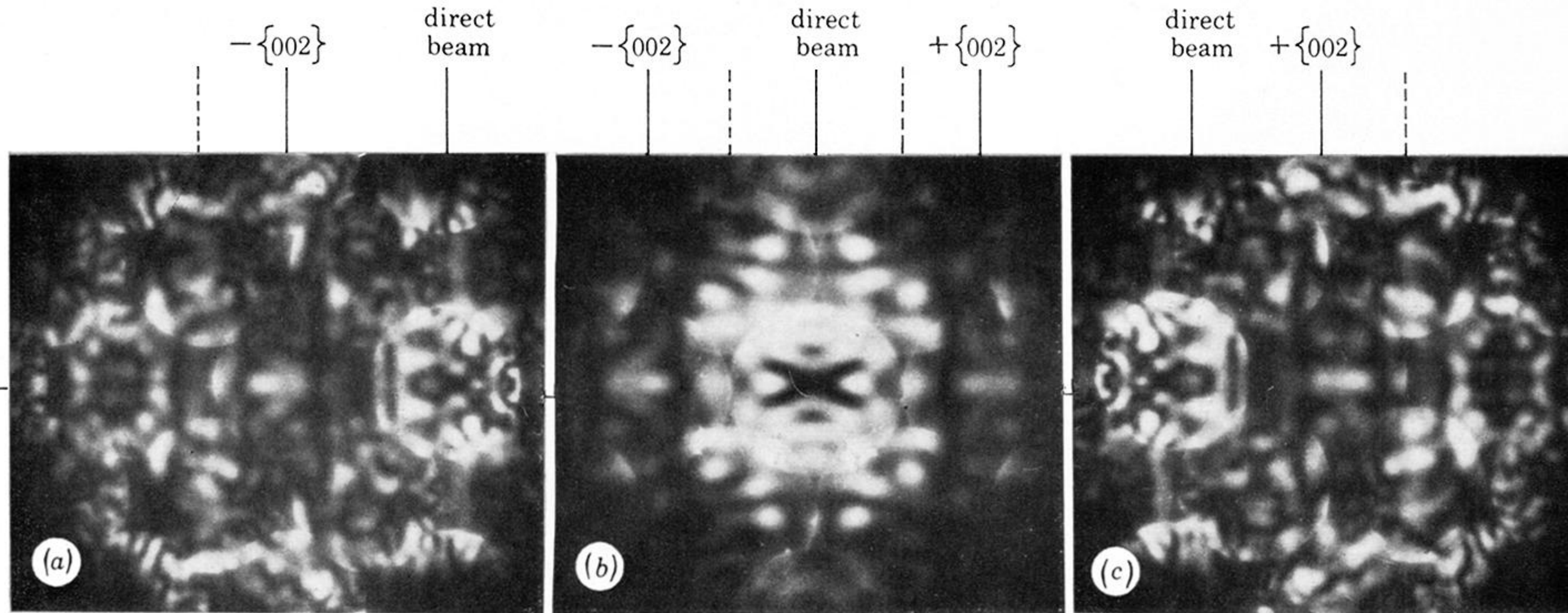
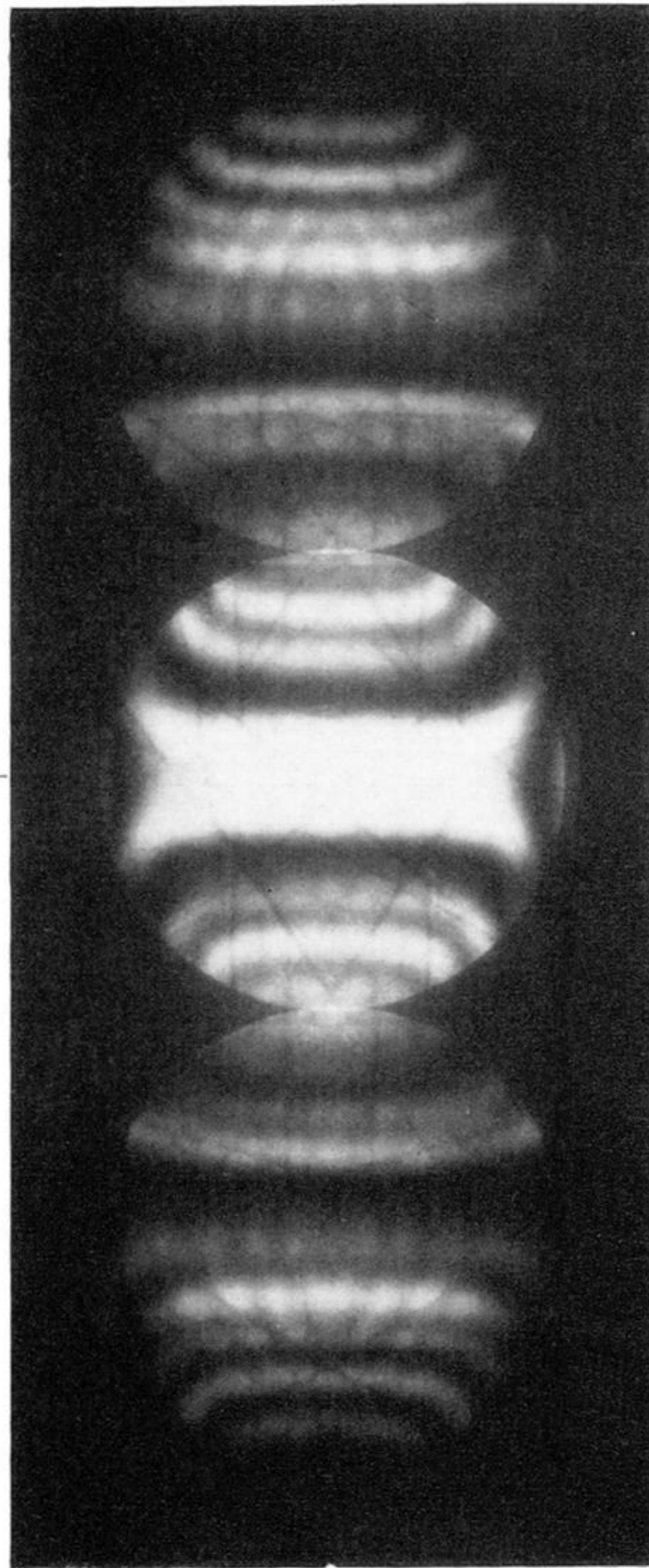


FIGURE 14. GaAs $\langle 110 \rangle$ convergent beam patterns from a $\{110\}$ foil taken at an operating voltage of 100 kV. There is axial illumination in (b); in (a) and (c) the image of the aperture has been shifted to the right and left respectively. The centres of the zero order and $\pm \{002\}$ disks are marked by the intersection of the solid vertical lines with the horizontal line. The dashed lines intersect the horizontal line at the $\pm \{002\}$ Bragg positions.

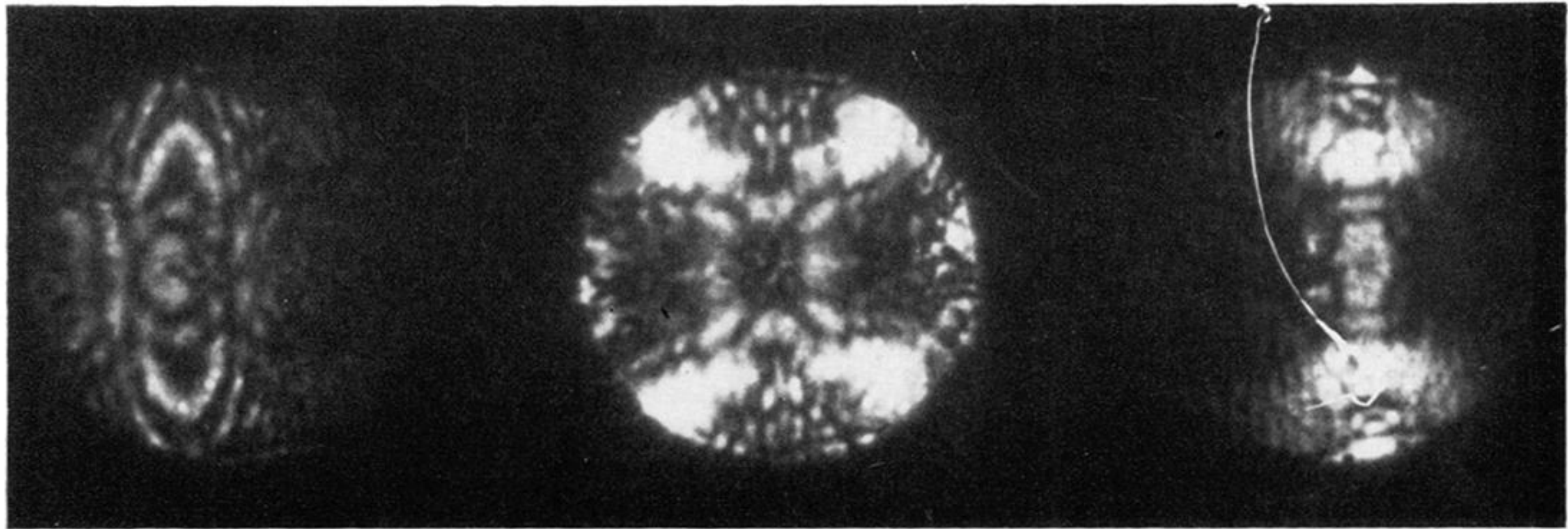
mirror line



Downloaded from rsta.royalsocietypublishing.org

mirror line

FIGURE 15. Si $\langle 211 \rangle$ axial convergent beam pattern from a $\{111\}$ foil taken at an operating voltage of approximately 96.5 kV. The broken horizontal line would be a mirror line in the projection approximation.



$-\{\bar{1}11\}$

zero beam

$+\{\bar{1}11\}$

FIGURE 16. Multiple dark-field image of gold $\langle 211 \rangle$ showing out-of-focus bend contours in each disk. The $\{111\}$ specimen has been tilted through 20° about the $\langle 0\bar{1}1 \rangle$ direction perpendicular to the line of the disks to obtain this pattern. Tables 4 and 2 predict 2 mm symmetry for the pattern but the tilted surfaces destroy the mirror line parallel to the tilt axis (M. D. Shannon, unpublished work).